

Partial wave analysis of the charmed baryon hadronic decay $\Lambda_c^+ \rightarrow \Lambda\pi^+\pi^0$



The BESIII collaboration

E-mail: besiii-publications@ihep.ac.cn

ABSTRACT: Based on e^+e^- collision samples corresponding to an integrated luminosity of 4.4 fb^{-1} collected with the BESIII detector at center-of-mass energies between 4.6 GeV and 4.7 GeV, a partial wave analysis of the charmed baryon hadronic decay $\Lambda_c^+ \rightarrow \Lambda\pi^+\pi^0$ is performed, and the decays $\Lambda_c^+ \rightarrow \Lambda\rho(770)^+$ and $\Lambda_c^+ \rightarrow \Sigma(1385)\pi$ are studied for the first time. Making use of the world-average branching fraction $\mathcal{B}(\Lambda_c^+ \rightarrow \Lambda\pi^+\pi^0)$, their branching fractions are determined to be

$$\begin{aligned}\mathcal{B}(\Lambda_c^+ \rightarrow \Lambda\rho(770)^+) &= (4.06 \pm 0.30 \pm 0.35 \pm 0.23) \times 10^{-2}, \\ \mathcal{B}(\Lambda_c^+ \rightarrow \Sigma(1385)^+\pi^0) &= (5.86 \pm 0.49 \pm 0.52 \pm 0.35) \times 10^{-3}, \\ \mathcal{B}(\Lambda_c^+ \rightarrow \Sigma(1385)^0\pi^+) &= (6.47 \pm 0.59 \pm 0.66 \pm 0.38) \times 10^{-3},\end{aligned}$$

where the first uncertainties are statistical, the second are systematic, and the third are from the uncertainties of the branching fractions $\mathcal{B}(\Lambda_c^+ \rightarrow \Lambda\pi^+\pi^0)$ and $\mathcal{B}(\Sigma(1385) \rightarrow \Lambda\pi)$. In addition, the decay asymmetry parameters are measured to be $\alpha_{\Lambda\rho(770)^+} = -0.763 \pm 0.053 \pm 0.045$, $\alpha_{\Sigma(1385)^+\pi^0} = -0.917 \pm 0.069 \pm 0.056$, and $\alpha_{\Sigma(1385)^0\pi^+} = -0.789 \pm 0.098 \pm 0.056$.

KEYWORDS: Branching fraction, Charm Physics, e^+e^- Experiments

ARXIV EPRINT: [2209.08464](https://arxiv.org/abs/2209.08464)

Contents

1	Introduction	1
2	BESIII experiment and Monte Carlo simulation	4
3	Event selection	5
4	Partial wave analysis	8
4.1	Helicity angle definitions	8
4.2	Helicity amplitude	8
4.3	Likelihood function construction and fit fraction	12
4.4	Nominal fit results	13
4.5	Decay asymmetry parameters	15
5	Systematic uncertainties	20
6	Summary	22
A	Alignment angle calculation	23
	The BESIII collaboration	29

1 Introduction

The charmed baryon Λ_c^+ was discovered 40 years ago [1] and has been designated as the ground state of the charmed baryons with spin-parity $J^P = \frac{1}{2}^+$ [2]. Recently, remarkable progress has been achieved in the study of hadronic weak decays of the charmed baryons, including absolute branching fraction (BF) measurements [3–5] and the re-ordering of the lifetime hierarchy [6–9]. The BESIII collaboration is presently one of the most active contributors to the measurements of the Λ_c^+ decay parameters [10]. The application of partial wave analysis (PWA) techniques to multi-body hadronic decays of the Λ_c^+ at BESIII is expected to fill the current lack of information about Λ_c^+ decays to an octet baryon and a vector meson, or a decuplet baryon and a pseudo-scalar meson [11]. For instance, the decays $\Lambda_c^+ \rightarrow \Sigma(1385)\pi$ and $\Lambda_c^+ \rightarrow \Lambda\rho(770)^+$ have not yet been observed [11], and only an upper limit has been reported by CLEO [12] assuming $\Lambda_c^+ \rightarrow \Lambda\rho(770)^+$ contributes 100% in the $\Lambda_c^+ \rightarrow \Lambda\pi^+\pi^0$ process. Therefore, the accurate measurements of these intermediate states will provide crucial information about the nature of charmed baryons.

In the field of theoretical calculations, much effort has been made in recent years to evaluate the non-perturbative contributions to the charmed baryon hadronic decays [3–5]. Based on different theoretical approaches [13–17], the BFs and decay asymmetry parameters

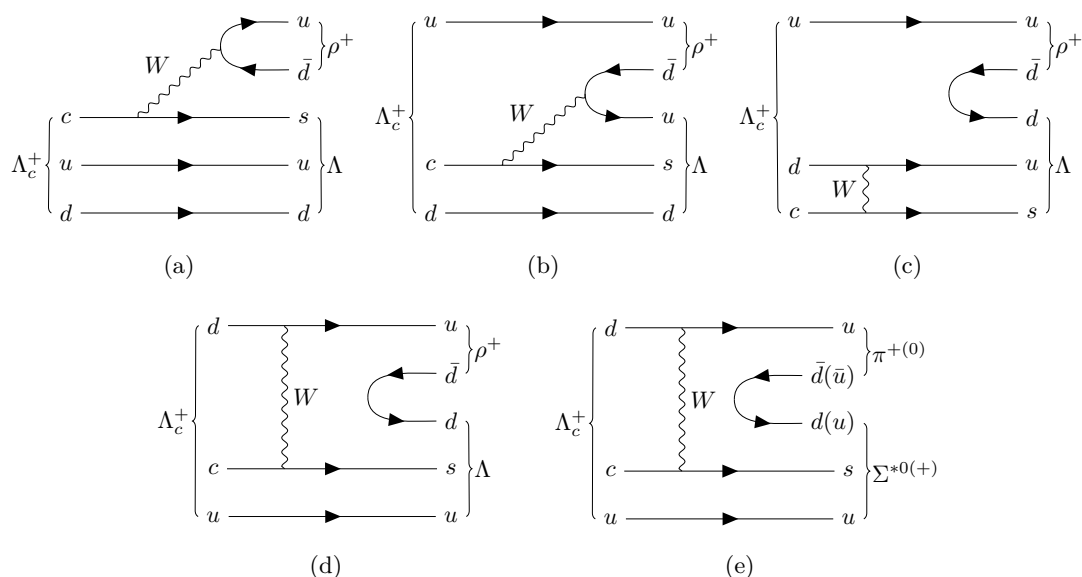


Figure 1. Topological diagrams for the decays $\Lambda_c^+ \rightarrow \Lambda\rho(770)^+$ (a)-(d) and $\Lambda_c^+ \rightarrow \Sigma(1385)\pi$ (e). The external W -emission diagram (a) corresponds to a factorizable amplitude, while the internal W -emission (b) and W -exchange diagrams (c)-(e) correspond to non-factorizable amplitudes. Here, the symbols ρ^+ and Σ^* denote $\rho(770)^+$ and $\Sigma(1385)$, respectively.

of the decays $\Lambda_c^+ \rightarrow \Lambda\rho(770)^+$ and $\Lambda_c^+ \rightarrow \Sigma(1385)\pi$ are predicted. Table 1 summarizes the theoretical predictions of the BFs of $\Lambda_c^+ \rightarrow \Lambda\rho(770)^+$ and $\Lambda_c^+ \rightarrow \Sigma(1385)\pi$, as well as the current world average published by the Particle Data Group (PDG). Remarkably, no experimental measurement is available so far.

For the decay $\Lambda_c^+ \rightarrow \Lambda\rho(770)^+$, both factorizable and non-factorizable diagrams will contribute to the amplitude [13]. The contributing topological diagrams are shown in figure 1(a)-(d), where the external W -emission diagram in figure 1(a) contributes as a factorizable amplitude and the internal W -emission in figure 1(b) and the W -exchange diagrams in figure 1(c) and (d) contribute as non-factorizable amplitudes. The BFs are related to the modulus squared of the sum of different topological amplitudes, and the decay asymmetry parameters are relevant to the interference of the internal partial wave amplitudes. In theoretical calculations, ref. [13] adopted an effective Hamiltonian with a factorization approach and $SU(3)_F$ symmetry, and refs. [14, 15] implemented the pole model, where the baryon decay amplitude is parameterized as baryon and meson pole contributions.

For the decay $\Lambda_c^+ \rightarrow \Sigma(1385)\pi$, only a non-factorizable contribution [16] is expected in the quark diagram scheme. The Λ_c^+ baryon has spin-parity $J^P = \frac{1}{2}^+$ and its valence quark structure consists of a charm quark and of a flavor anti-symmetric ud diquark component. The constituent quarks of the $\Sigma(1385)$ baryon, instead, have a fully symmetric flavor structure, due to its spin-parity $J^P = \frac{3}{2}^+$. Hence, the external W -emission diagram similar to figure 1(a) is forbidden in this decay. According to the Körner-Pati-Woo theorem [18–21], the quark pair, which is produced through the weak interaction and then confined into a

	Theoretical calculation				PDG
	Ref. [13]	Refs. [14, 15]	Ref. [16]	Ref. [17]	
$10^2 \times \mathcal{B}(\Lambda_c^+ \rightarrow \Lambda\rho(770)^+)$	4.81 ± 0.58	4.0	—	—	< 6
$10^3 \times \mathcal{B}(\Lambda_c^+ \rightarrow \Sigma(1385)^+\pi^0)$	—	—	2.8 ± 0.4	2.2 ± 0.4	—
$10^3 \times \mathcal{B}(\Lambda_c^+ \rightarrow \Sigma(1385)^0\pi^+)$	—	—	2.8 ± 0.4	2.2 ± 0.4	—
$\alpha_{\Lambda\rho(770)^+}$	-0.27 ± 0.04	-0.32	—	—	—
$\alpha_{\Sigma(1385)^+\pi^0}$	—	—	—	$-0.91^{+0.45}_{-0.10}$	—
$\alpha_{\Sigma(1385)^0\pi^+}$	—	—	—	$-0.91^{+0.45}_{-0.10}$	—

Table 1. Various theoretical calculations of BFs and decay asymmetry parameters of the decays $\Lambda_c^+ \rightarrow \Lambda\rho(770)^+$ and $\Lambda_c^+ \rightarrow \Sigma(1385)\pi$. Reference [13] adopted the effective Hamiltonian with factorization approach and $SU(3)_F$ symmetry, refs. [14, 15] implemented the pole model, ref. [16] considered the quark diagram scheme and ref. [17] used the effective Hamiltonian with $SU(3)_F$ symmetry. The current experimental measurement is from the PDG [11], and “—” means unavailable.

baryon, is flavor anti-symmetric and is not allowed in the $\Sigma(1385)$ quark structure. Therefore, the internal W -emission and one of the W -exchange diagrams, similar to figure 1(b) and (c), are also suppressed in this decay. As a consequence, only the W -exchange diagram in figure 1(e) contributes to the decay $\Lambda_c^+ \rightarrow \Sigma(1385)\pi$, which is a pure non-factorizable contribution. In ref. [16] the BFs are calculated through the quark diagram scheme, while in ref. [17] the BFs along with decay asymmetry parameters are determined on the basis of an effective Hamiltonian with $SU(3)_F$ symmetry.

Since the non-factorizable contribution is more difficult to treat than the factorizable one in the theoretical calculations, detailed study of the complicated $\Lambda_c^+ \rightarrow \Lambda\rho(770)^+$ process and the pure non-factorizable $\Lambda_c^+ \rightarrow \Sigma(1385)\pi$ process will provide important inputs to improve the theoretical calculation. Thus, in this paper, the first PWA of the charmed baryon hadronic decay $\Lambda_c^+ \rightarrow \Lambda\pi^+\pi^0$ is reported. The analysis is performed on e^+e^- collision data samples with a total integrated luminosity of 4.4 fb^{-1} [22, 23] collected at center-of-mass (c.m.) energies \sqrt{s} between 4.6 and 4.7 GeV with the BESIII detector [24] at the BEPCII [25] collider. The luminosities at each c.m. energy are listed in table 2. From the PWA results, the fit fractions (FFs) and the partial wave amplitudes of intermediate resonances can be derived. Combining the FFs with the average value of $\mathcal{B}(\Lambda_c^+ \rightarrow \Lambda\pi^+\pi^0) = (7.1 \pm 0.4)\%$ from the PDG [11], the BFs for the decays $\Lambda_c^+ \rightarrow \Lambda\rho(770)^+$ and $\Lambda_c^+ \rightarrow \Sigma(1385)\pi$ are determined for the first time. In addition, using the partial wave amplitudes obtained in the PWA, the corresponding decay asymmetry parameters are determined for the first time. They will provide useful information for testing theoretical calculations, especially for the descriptions of the interference effects among the internal different partial waves [26, 27]. Charge conjugation is implied throughout this paper unless mentioned explicitly otherwise.

\sqrt{s} (GeV)	Luminosity (pb^{-1})
4.600	$586.9 \pm 0.1 \pm 3.9$
4.612	$103.8 \pm 0.1 \pm 0.6$
4.628	$521.5 \pm 0.1 \pm 2.8$
4.641	$552.4 \pm 0.1 \pm 2.9$
4.661	$529.6 \pm 0.1 \pm 2.8$
4.682	$1669.3 \pm 0.2 \pm 8.8$
4.699	$536.4 \pm 0.1 \pm 2.8$

Table 2. The c.m. energies and integrated luminosities for the data samples [22, 23].

2 BESIII experiment and Monte Carlo simulation

The BESIII detector [24] records symmetric e^+e^- collisions provided by the BEPCII storage ring [25], which operates at c.m energies ranging from 2.0 to 4.95 GeV, with a peak luminosity of $1 \times 10^{33} \text{ cm}^{-2}\text{s}^{-1}$ achieved at $\sqrt{s} = 3.77 \text{ GeV}$. The BESIII detector has collected large data samples in this energy region [28]. The cylindrical core of the BESIII detector covers 93% of the full solid angle and consists of a helium-based multilayer drift chamber (MDC), a plastic scintillator time-of-flight system (TOF), and a CsI(Tl) electromagnetic calorimeter (EMC), which are all enclosed in a superconducting solenoidal magnet providing a 1.0 T magnetic field. The solenoid is supported by an octagonal flux-return yoke with resistive plate counter muon identification modules interleaved with steel. The charged-particle momentum resolution at 1 GeV/c is 0.5%, and the dE/dx resolution is 6% for electrons from Bhabha scattering. The EMC measures photon energies with a resolution of 2.5% (5%) at 1 GeV in the barrel (end cap) region. The time resolution in the TOF barrel region is 68 ps, while that in the end cap region was initially 110 ps. The end cap TOF system was upgraded in 2015 using multi-gap resistive plate chamber technology, providing a time resolution of 60 ps [29–31].

Simulated samples produced with GEANT4-based [32] Monte Carlo (MC) software, which includes the geometric description of the BESIII detector and the detector response performance [33–35], are used to determine detection efficiencies and to estimate background contributions. The simulation describes the beam energy spread and initial state radiation (ISR) in the e^+e^- annihilations with the generator KKMC [36, 37]. The inclusive MC samples, corresponding to around 40 times of the number of events of the data samples, include the production of $\Lambda_c^+\bar{\Lambda}_c^-$ pairs, open charm processes, the ISR production of vector charmonium(-like) states, and the continuum processes incorporated in KKMC [36, 37]. The known decay modes are modelled with EVTGEN [38, 39] using BFs taken from the PDG [11] and the remaining unknown charmonium decays are modelled with LUNDCHARM [40, 41]. Final state radiation from charged final state particles is incorporated using PHOTOS [42]. The MC samples of the signal process $\Lambda_c^+ \rightarrow \Lambda\pi^+\pi^0$ are produced with a uniform phase-space distribution (PHSP). At each c.m. energy point 800k events are generated, except at 4.682 GeV, where the sample consists of 1.6M events to reflect the larger integrated luminosity of the data set.

3 Event selection

The e^+e^- collision energies of the data sets are just above the production threshold of the $\Lambda_c^+\bar{\Lambda}_c^-$ pair, providing a clean environment without additional accompanying hadrons. Taking advantage of the threshold pair production and of the excellent performance of the BESIII detector, a single-tag strategy is used, where only one charmed baryon decay is reconstructed (Λ_c^+), improving the detection efficiency and, therefore, providing a larger data sample. The signal candidates for $\Lambda_c^+ \rightarrow \Lambda\pi^+\pi^0$ are reconstructed from combinations of charged tracks and photon candidates recorded by the detector that satisfy the following selection criteria.

Charged particle tracks detected in the MDC are required to have a polar angle θ in the range of $|\cos\theta| < 0.93$, where θ is defined with respect to the z -axis, which is the symmetry axis of the MDC. For charged tracks not originating from Λ decays, the distance of the closest approach to the interaction point (IP) is required to be less than 10 cm along the z -axis (V_z), and to be less than 1 cm in the perpendicular plane (V_r). Particle identification (PID) for charged tracks is implemented by combining the information of specific ionization energy loss in the MDC (dE/dx) and the time of flight measured in the TOF into a likelihood value $\mathcal{L}(h)$ for each hadron h hypothesis, where $h = p, K, \text{ or } \pi$. Charged tracks are identified as protons if the proton hypothesis has the greatest likelihood ($\mathcal{L}(p) > \mathcal{L}(K)$ and $\mathcal{L}(p) > \mathcal{L}(\pi)$), or as pions if satisfying $\mathcal{L}(\pi) > \mathcal{L}(K)$.

Photon candidates from π^0 decays are reconstructed using electromagnetic showers in the EMC. The deposited energy of each shower is required to be larger than 25 MeV in the barrel region ($|\cos\theta| < 0.80$) and larger than 50 MeV in the end cap region ($0.86 < |\cos\theta| < 0.92$). To reject fake photons arising from electronic noise, beam background, and showers unrelated to the event, the difference between the EMC time and the event start time [43] is required to be within 700 ns. For π^0 candidates, the invariant mass of the photon pair is required to be within $0.115 < M_{\gamma\gamma} < 0.150 \text{ GeV}/c^2$. To further improve the momentum resolution, a one-constraint (1C) kinematic fit is performed by constraining the invariant mass of the photon pair to the nominal π^0 mass [11]. The updated momentum will be used in the further analysis.

The Λ candidates are reconstructed with two oppositely charged tracks identified as p and π^- . The tracks are required to satisfy $V_z < 20 \text{ cm}$, and no V_r requirement is imposed. For proton, the previous mentioned PID requirement is applied, while for pion, it is not. The $p\pi^-$ pairs are constrained to originate from a common vertex by requiring the χ^2 of a vertex fit to be less than 100. An additional fit is performed by constraining the momentum of $p\pi^-$ pair to be aligned with the direction from the IP to the Λ decay vertex, and the fitted decay length is required to be larger than twice its uncertainty. Furthermore, the invariant mass is required to be within $1.111 < M_{p\pi^-} < 1.121 \text{ GeV}/c^2$.

If an event satisfies both the above $\Lambda_c^+ \rightarrow \Lambda\pi^+\pi^0$ selection criteria and $\Lambda_c^+ \rightarrow \Sigma^0\pi^+$ selection criteria, it will be rejected to veto $M_{\Lambda\pi^+}$ peaking background arising from $\Lambda_c^+ \rightarrow \Sigma^0\pi^+$ decay. Here, the $\Lambda_c^+ \rightarrow \Sigma^0\pi^+$ selection criteria consist of selecting π^+ , Λ and γ candidates where the combination $\Lambda\gamma$ is required to be within Σ^0 mass window $1.179 < M_{\Lambda\gamma} < 1.203 \text{ GeV}/c^2$, as described in detail in ref. [10]. After applying these selections, no peaking background is found in data, while only 1.6% signal detection efficiency is lost, as evaluated in the inclusive MC samples.

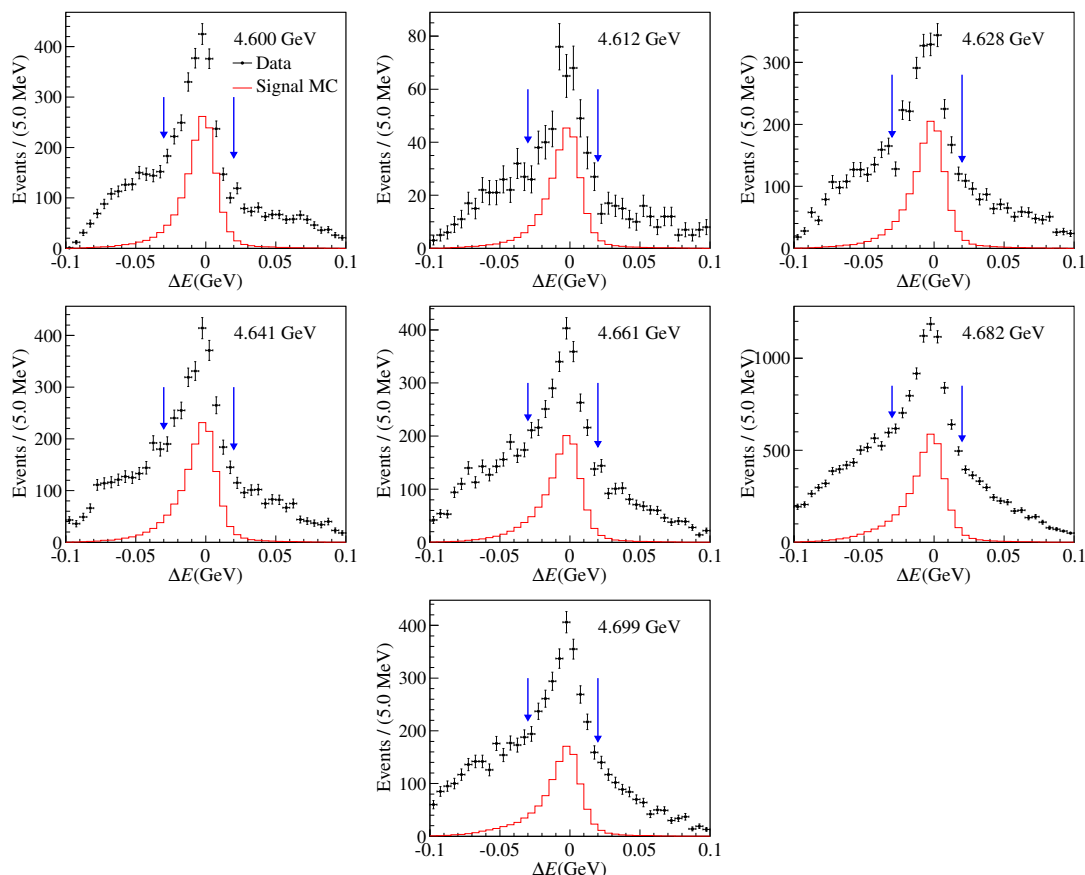


Figure 2. The ΔE distributions of data (dots with error bars) and signal MC samples (thick lines) at seven energy points for $\Lambda_c^+ \rightarrow \Lambda\pi^+\pi^0$ decay. The blue arrows indicate the ΔE selection region. The signal MC samples are presented in arbitrary scale for illustration.

To further select the signal candidates, the beam-constrained mass M_{BC} and the energy difference ΔE are used, defined as

$$M_{\text{BC}} \equiv \sqrt{E_{\text{beam}}^2/c^4 - |\vec{p}|^2/c^2} \quad (3.1)$$

and

$$\Delta E \equiv E - E_{\text{beam}}, \quad (3.2)$$

where E_{beam} is the beam energy, \vec{p} and E are the reconstructed momentum and energy of the signal candidate, respectively. Signal candidates are expected to have M_{BC} and ΔE consistent with the nominal Λ_c^+ mass [11] and zero, respectively. The combination with the minimum $|\Delta E|$ is considered as the Λ_c^+ candidate and its ΔE is required to satisfy $-0.03 < \Delta E < 0.02$ GeV. The ΔE distributions of data and signal MC samples are shown in figure 2.

An extended un-binned maximum likelihood fit is performed on the M_{BC} distribution of each energy point, as shown in figure 3, in order to determine the signal and background yields. In the fit, the signal shape is derived from the kernel-estimated non-parametric

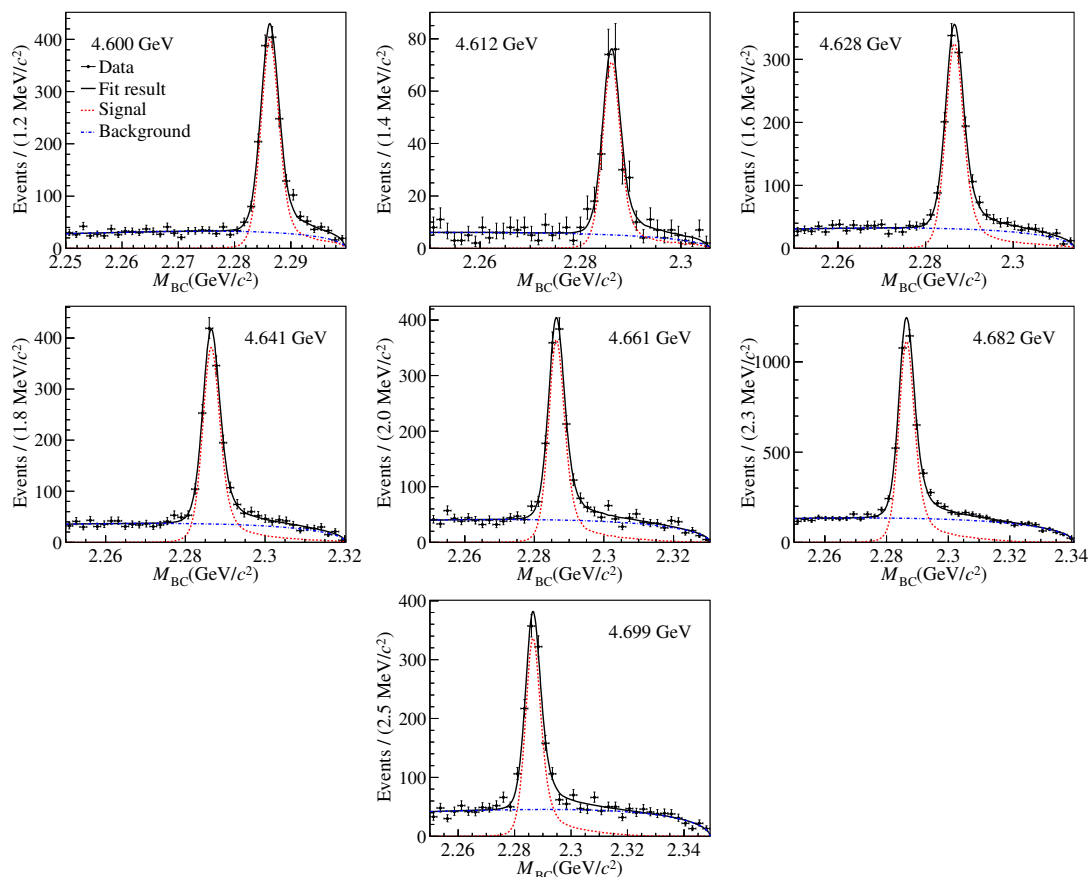


Figure 3. Fits to the M_{BC} distributions at each energy point for the $\Lambda_c^+ \rightarrow \Lambda \pi^+ \pi^0$ decay. The dots with error bars are data, the (black) solid curve is the fit function, which is the sum of the signal shape (red dashed curve) and the background shape (blue dash-dotted curve). No obvious peaking background is observed.

shape [44] based on PHSP MC samples convolved with a Gaussian function, to account for the difference between data and MC simulation caused by imperfect modelling of the detector resolution and beam-energy spread. The parameters of the Gaussian function are left free in the fit. The background shape is modelled by an ARGUS function [45] defined as

$$f(M_{BC}, E_0, c, p) = M_{BC} \left(1 - \left(\frac{M_{BC}}{E_0} \right)^2 \right)^p \times e^{c \left(1 - \frac{M_{BC}}{E_0} \right)^2}, \quad (3.3)$$

where E_0 is the endpoint of M_{BC} and is fixed to the beam energy, p is the power parameter and is equal to 0.5, and c is a free parameter in the fit. The global probability density function consists of a linear combination of signal and background contributions. The fit results, the M_{BC} signal regions, as well as the signal purities and background fractions are listed in table 3. Events within the M_{BC} signal region are considered as signal candidates in the further PWA fit, and the events underlying the M_{BC} sideband region $2.25 < M_{BC} < 2.27 \text{ GeV}/c^2$ are considered as background events. At each energy point, the signal purity within the M_{BC} signal region is larger than 80%, which is sufficient to perform a reliable partial wave analysis.

\sqrt{s} (GeV)	M_{BC} requirement (GeV/ c^2)	Signal yield	Bkg yield	Purity (%)	Bkg fraction (%)
4.600	(2.282, 2.291)	1351 ± 43	217.4 ± 8.2	86.1 ± 0.7	13.9 ± 0.7
4.612	(2.282, 2.291)	233 ± 17	32.8 ± 2.9	87.7 ± 1.4	12.3 ± 1.4
4.628	(2.282, 2.291)	1040 ± 37	174.2 ± 6.7	85.7 ± 0.8	14.3 ± 0.8
4.641	(2.282, 2.292)	1200 ± 39	203.5 ± 7.1	85.5 ± 0.7	14.5 ± 0.7
4.661	(2.282, 2.292)	1047 ± 35	199.1 ± 6.3	84.0 ± 0.7	16.0 ± 0.7
4.682	(2.282, 2.293)	3120 ± 63	642 ± 11	82.9 ± 0.4	17.1 ± 0.4
4.699	(2.282, 2.293)	906 ± 34	201.4 ± 5.9	81.8 ± 0.8	18.2 ± 0.8

Table 3. The results of signal and background (Bkg) yields in the M_{BC} signal region at seven energy points, along with M_{BC} requirement boundaries, signal purities and background fractions. The M_{BC} requirement is applied to improve the signal purities.

4 Partial wave analysis

After applying all the selection criteria mentioned above, around 10k signal events are selected in data and can be used to fit the helicity amplitude of the $\Lambda_c^+ \rightarrow \Lambda\pi^+\pi^0$ decay. To improve the momentum resolution, an additional 3C kinematic fit under the hypothesis of $e^+e^- \rightarrow \Lambda_c^+(\rightarrow \Lambda\pi^+\pi^0)\bar{\Lambda}_c^-$ is performed with the $p\pi^-$ system constrained to the nominal Λ mass, the $\Lambda\pi^+\pi^0$ constrained to the Λ_c^+ mass and the recoil mass against $\Lambda\pi^+\pi^0$ constrained to the Λ_c^+ mass.

In this work, the decay amplitude is constructed using the helicity amplitude formalism, and the full procedure is implemented based on the open-source framework called TF-PWA [46]. The amplitude is defined in the Λ_c^+ rest frame to which all final state particles are boosted. Parameters describing the amplitude of the $\bar{\Lambda}_c^-$ decay are related to those of Λ_c^+ by performing a parity transformation on the $\bar{\Lambda}_c^-$ candidates, under the assumption of CP conservation.

4.1 Helicity angle definitions

The full decay amplitude of $\Lambda_c^+ \rightarrow \Lambda\pi^+\pi^0$ consists of three decay chains:

- $\Lambda_c^+ \rightarrow \Lambda\rho(770)^+(\theta_{\Lambda_c^+}^1), \rho(770)^+ \rightarrow \pi^+\pi^0(\theta_{\rho^+}, \phi_{\pi^0}^{\rho^+}), \Lambda \rightarrow p\pi^-(\theta_{\Lambda_1}, \phi_p^{\Lambda_1}),$
- $\Lambda_c^+ \rightarrow \Sigma^{*+}\pi^0(\theta_{\Lambda_c^+}^2), \Sigma^{*+} \rightarrow \Lambda\pi^+(\theta_{\Sigma^{*+}}, \phi_{\Lambda}^{\Sigma^{*+}}), \Lambda \rightarrow p\pi^-(\theta_{\Lambda_2}, \phi_p^{\Lambda_2}),$
- $\Lambda_c^+ \rightarrow \Sigma^{*0}\pi^+(\theta_{\Lambda_c^+}^3), \Sigma^{*0} \rightarrow \Lambda\pi^0(\theta_{\Sigma^{*0}}, \phi_{\Lambda}^{\Sigma^{*0}}), \Lambda \rightarrow p\pi^-(\theta_{\Lambda_3}, \phi_p^{\Lambda_3}).$

The corresponding helicity angle definitions are shown in figure 4.

4.2 Helicity amplitude

To construct the full decay amplitude of the decay $\Lambda_c^+ \rightarrow \Lambda\pi^+\pi^0$, the helicity formalism is used based on the Isobar model describing the three-body decay as a two-step sequential quasi-two-body decay. For each two-body decay $0 \rightarrow 1 + 2$, the helicity amplitude can be written as

$$A_{\lambda_0, \lambda_1, \lambda_2}^{0 \rightarrow 1+2} = H_{\lambda_1, \lambda_2}^{0 \rightarrow 1+2} D_{\lambda_0, \lambda_1 - \lambda_2}^{J_0^*}(\phi, \theta, 0), \quad (4.1)$$

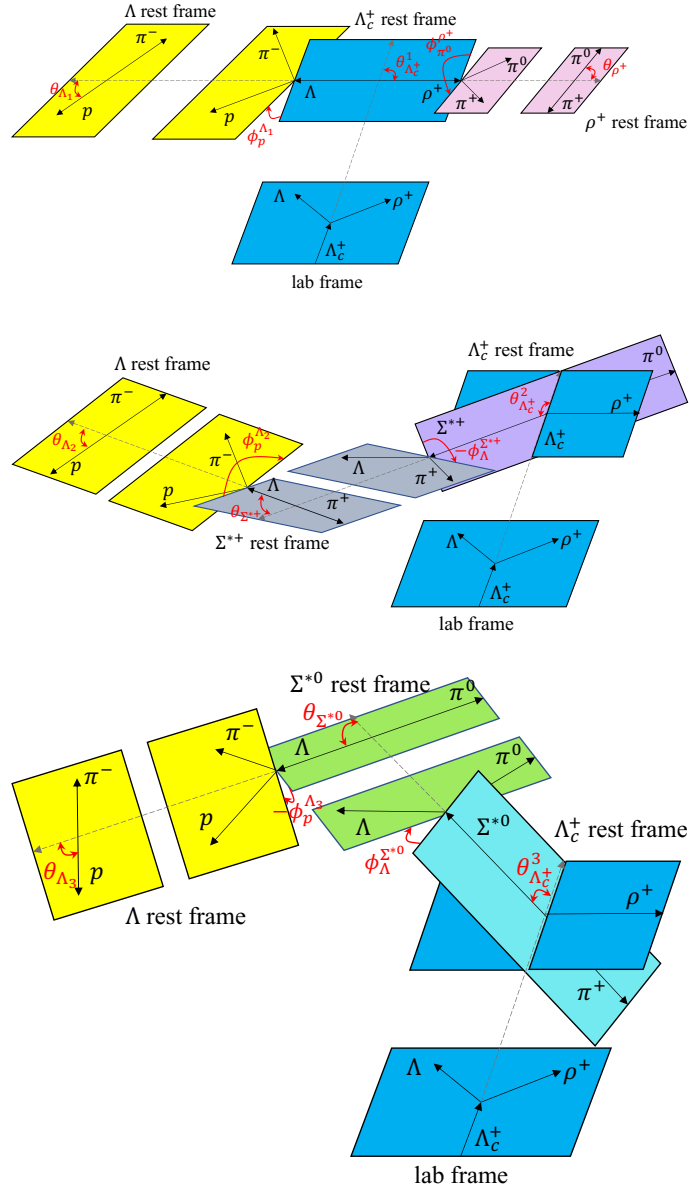


Figure 4. Definitions for the helicity angles with different decay chains in the decay $\Lambda_c^+ \rightarrow \Lambda\pi^+\pi^0$. The notation θ_R denotes the θ helicity angle of the decay of resonance R . For the Λ_c^+ helicity angle, the superscripts 1, 2, and 3 are used to differentiate three decay chains. The notation ϕ_B^A denotes the ϕ helicity angle between the plane of B and the plane of its mother particle A . In convention, the right-hand frame is chosen as the normal direction for a ϕ rotation, and the anti-direction rotation is denoted as $-\phi$ in the figure. In addition, the subscripts 1, 2, and 3 for Λ are also used to differentiate three decay chains. The exact calculations of different helicity angles are implemented according to the conventions in ref. [47].

where the amplitude $H_{\lambda_1, \lambda_2}^{0 \rightarrow 1+2}$ is given by the LS coupling formula [48] along with barrier factor terms

$$H_{\lambda_1, \lambda_2}^{0 \rightarrow 1+2} = \sum_{l_s} g_{l_s} \sqrt{\frac{2l+1}{2J_0+1}} \langle l_0, s\delta | J_0, \delta \rangle \langle J_1 J_2, \lambda_1 - \lambda_2 | s, \delta \rangle \left(\frac{q}{q_0}\right)^l B'_l(q, q_0, d), \quad (4.2)$$

where g_{l_s} is the partial wave amplitude, $J_{0,1,2}$ are the spins of the particles 0, 1, and 2, $\lambda_{1,2}$ are the helicities for the particles 1 and 2, and $\delta = \lambda_1 - \lambda_2$ is the helicity difference. Here, q is the three-momentum modulus of particle 1 in the rest frame of particle 0, which is calculated as

$$q = \frac{\sqrt{[m^2 - (m_1 + m_2)^2][m^2 - (m_1 - m_2)^2]}}{2m}, \quad (4.3)$$

where m , m_1 and m_2 are the masses of the particles 0, 1, and 2, respectively. The normalization factor q_0 is calculated at the nominal resonance mass. The factor $B'_l(q, q_0, d)$ is the reduced Blatt-Weisskopf barrier factor [49], which is explicitly expressed as

$$\begin{aligned} B'_0(q, q_0, d) &= 1, \\ B'_1(q, q_0, d) &= \sqrt{\frac{1 + (q_0 d)^2}{1 + (q d)^2}}, \\ B'_2(q, q_0, d) &= \sqrt{\frac{9 + 3(q_0 d)^2 + (q_0 d)^4}{9 + 3(q d)^2 + (q d)^4}}, \\ B'_3(q, q_0, d) &= \sqrt{\frac{225 + 45(q_0 d)^2 + 6(q_0 d)^4 + (q_0 d)^6}{225 + 45(q d)^2 + 6(q d)^4 + (q d)^6}}, \\ B'_4(q, q_0, d) &= \sqrt{\frac{11025 + 1575(q_0 d)^2 + 135(q_0 d)^4 + 10(q_0 d)^6 + (q_0 d)^8}{11025 + 1575(q d)^2 + 135(q d)^4 + 10(q d)^6 + (q d)^8}}. \end{aligned} \quad (4.4)$$

In the Wigner D -function, $D_{\lambda_0, \lambda_1 - \lambda_2}^{J_0^*}(\phi, \theta, 0)$, ϕ and θ are helicity angles, and are shown in figure 4. The definitions can be found in ref. [47]. In eq. (4.4), the radius d is chosen as $d = 0.73$ fm, which is the same as in ref. [50].

The amplitude for a complete decay chain is constructed as the product of each two body decay amplitude and the resonant propagator R . For example, in the sequential decay $\Lambda_c^+ \rightarrow \Lambda \rho(770)^+$, $\rho(770)^+ \rightarrow \pi^+ \pi^0$, $\Lambda \rightarrow p \pi^-$, the amplitude is written as

$$A_{\lambda_{\Lambda_c^+}, \lambda_p}^\rho = \sum_{\lambda_\rho, \lambda_\Lambda} A_{\lambda_{\Lambda_c^+}, \lambda_\rho, \lambda_\Lambda}^{\Lambda_c^+ \rightarrow \rho \Lambda} R_\rho(M_{\pi^+ \pi^0}) A_{\lambda_\rho, 0, 0}^{\rho \rightarrow \pi^+ \pi^0} A_{\lambda_\Lambda, \lambda_p, 0}^{\Lambda \rightarrow p \pi^-}. \quad (4.5)$$

For the non-resonant (NR) decay, the amplitude $A_{\lambda_{\Lambda_c^+}, \lambda_p}^{NR}$ is replaced by setting $R_{NR}(M_{\pi^+ \pi^0})$ as unity, expressed as

$$A_{\lambda_{\Lambda_c^+}, \lambda_p}^{NR} = \sum_{\lambda_{NR}, \lambda_\Lambda} A_{\lambda_{\Lambda_c^+}, \lambda_{NR}, \lambda_\Lambda}^{\Lambda_c^+ \rightarrow NR + \Lambda} A_{\lambda_{NR}, 0, 0}^{NR \rightarrow \pi^+ \pi^0} A_{\lambda_\Lambda, \lambda_p, 0}^{\Lambda \rightarrow p \pi^-}. \quad (4.6)$$

For the decay via the Σ^* intermediate states, the amplitude reads

$$A_{\lambda_{\Lambda_c^+}, \lambda_p}^{\Sigma^*} = \sum_{\lambda_{\Sigma^*}, \lambda_\Lambda} A_{\lambda_{\Lambda_c^+}, \lambda_{\Sigma^*}, 0}^{\Lambda_c^+ \rightarrow \Sigma^* \pi} R_{\Sigma^*}(M_{\Lambda \pi}) A_{\lambda_{\Sigma^*}, \lambda_\Lambda, 0}^{\Sigma^* \rightarrow \Lambda \pi} A_{\lambda_\Lambda, \lambda_p, 0}^{\Lambda \rightarrow p \pi^-}. \quad (4.7)$$

The propagator R includes different models. For Σ^* resonances, the relativistic Breit-Wigner formula is taken as

$$R_{\Sigma^*}(m) = \frac{1}{m_0^2 - m^2 - im_0\Gamma(m)}, \quad (4.8)$$

where the mass dependent width is

$$\Gamma(m) = \Gamma_0 \left(\frac{q}{q_0}\right)^{2l+1} \frac{m_0}{m} B_l'^2(q, q_0, d). \quad (4.9)$$

For the $\rho(770)^+$ resonance, the Gounaris-Sakurai (GS) model [51] is used:

$$R_\rho(m) = \frac{1 + D\Gamma_0/m_0}{(m_0^2 - m^2) + f(m) - im_0\Gamma(m)}, \quad (4.10)$$

where the mass dependent width $\Gamma(m)$ is defined with the same parametrization as eq. (4.9), and $f(m)$ and D are defined as

$$f(m) = \Gamma_0 \frac{m_0^2}{q_0^3} \left[q^2 [h(m) - h(m_0)] + (m_0^2 - m^2) q_0^2 \frac{dh}{dm} \Big|_{m_0} \right], \quad (4.11)$$

$$h(m) = \frac{2}{\pi} \frac{q}{m} \ln \left(\frac{m + 2q}{2m_\pi} \right), \quad (4.12)$$

$$\frac{dh}{dm} \Big|_{m_0} = h(m_0) \left[(8q_0^2)^{-1} - (2m_0^2)^{-1} \right] + (2\pi m_0^2)^{-1}, \quad (4.13)$$

$$D = \frac{f(0)}{\Gamma_0 m_0} = \frac{3}{\pi} \frac{m_\pi^2}{q_0^2} \ln \left(\frac{m_0 + 2q_0}{2m_\pi} \right) + \frac{m_0}{2\pi q_0} - \frac{m_\pi^2 m_0}{\pi q_0^3}. \quad (4.14)$$

The full amplitude is the coherent sum of all possible resonances and NR amplitudes, given as

$$\begin{aligned} \mathcal{A}_{\lambda_{\Lambda_c^+}, \lambda_p} &= \left(A_{\lambda_{\Lambda_c^+}, \lambda_p}^\rho + A_{\lambda_{\Lambda_c^+}, \lambda_p}^{NR} \right) \\ &+ \sum_{\lambda_p'} \left(\sum A_{\lambda_{\Lambda_c^+}, \lambda_p'}^{\Sigma^{*+}} \right) D_{\lambda_p', \lambda_p}^{1/2}(\alpha_p, \beta_p, \gamma_p) \\ &+ \sum_{\lambda_p'} \left(\sum A_{\lambda_{\Lambda_c^+}, \lambda_p'}^{\Sigma^{*0}} \right) D_{\lambda_p', \lambda_p}^{1/2}(\alpha_p', \beta_p', \gamma_p'), \end{aligned} \quad (4.15)$$

where the extra alignment D -functions are added to align the helicities of the final state protons. The details of the alignment angle calculations can be found in appendix A and in ref. [47].

For simplicity in the PWA fit, an overall resonance amplitude for each component term in eq. (4.15), as those listed in table 4, can be derived to represent the overall magnitude and phase of the specific component, while in each cascade process, one of partial wave amplitudes g_{ls} can be taken as reference amplitude with fixed amplitude of constant 1 (as the fixed amplitudes listed in table 5). Hence, the relative magnitudes and phases of the other partial wave amplitudes in each cascade process (as the free amplitudes listed in table 5) are left free in the fit.

4.3 Likelihood function construction and fit fraction

The probability density function for a given event is constructed using the full amplitude as

$$P = \frac{|\mathcal{A}|^2}{\int |\mathcal{A}|^2 d\Phi}, \quad |\mathcal{A}|^2 = \frac{1}{2} \sum_{\lambda_{\Lambda_c^+}, \lambda_p} |\mathcal{A}_{\lambda_{\Lambda_c^+}, \lambda_p}|^2, \quad (4.16)$$

where the factor $1/2$ arises from the average of the initial Λ_c^+ spin under the assumption of non polarization. Possible polarization effects are considered with the systematic uncertainties. The integration is calculated with a MC method via sufficiently large PHSP samples passing the simulated detector reconstruction stage, and we have

$$\int |\mathcal{A}|^2 d\Phi \propto \frac{1}{N_{\text{PHSP}}} \sum_{i \in \text{PHSP}} |\mathcal{A}(x_i)|^2. \quad (4.17)$$

The negative log likelihood (NLL) is constructed by summing all signal candidates and subtracting the M_{BC} sideband backgrounds

$$-\ln L = -\alpha \left[\sum_{i \in \text{data}} \ln P(x_i) - w'_{\text{bkg}} \sum_{i \in \text{sideband}} \ln P(x_i) \right], \quad (4.18)$$

where $w'_{\text{bkg}} = w_{\text{bkg}} \cdot \frac{N_{\text{data}}}{N_{\text{sideband}}}$, w_{bkg} is the background fraction listed in table 3, N_{data} and N_{sideband} are the events in the M_{BC} signal region and sideband region, respectively. To achieve an unbiased uncertainty estimation, the normalization factor derived from ref. [52] is taken into account, expressed as

$$\alpha = \frac{N_{\text{data}} - N_{\text{sideband}} w'_{\text{bkg}}}{N_{\text{data}} + N_{\text{sideband}} w'_{\text{bkg}}}. \quad (4.19)$$

An individual NLL is first constructed separately for a given energy point, and the joint NLL is obtained by summing over the NLL values of the different energy points. After minimizing the joint NLL, the parameter error matrix is calculated by the inverse of the Hessian matrix

$$V_{ij}^{-1} = -\frac{\partial^2 \ln L}{\partial X_i \partial X_j}, \quad (4.20)$$

where X_i is the i -th floating parameter in the fit.

The fit fraction (FF) for each resonant component can be calculated as

$$\text{FF}_i = \frac{\int |\mathcal{A}_i|^2 d\Phi'}{\int |\sum_k \mathcal{A}_k|^2 d\Phi'}, \quad (4.21)$$

where \mathcal{A}_i is the amplitude of the i -th component and the integration is calculated by the sum of truth level PHSP MC samples before requiring detector acceptance. Hence, the FFs of the interference part can be calculated as

$$\text{FF}_{i,j} = \frac{\int |\mathcal{A}_i + \mathcal{A}_j|^2 d\Phi'}{\int |\sum_k \mathcal{A}_k|^2 d\Phi'} - \text{FF}_i - \text{FF}_j. \quad (4.22)$$

Process	Magnitude	Phase ϕ (rad)	FF (%)	Significance
$\Lambda\rho(770)^+$	1.0 (fixed)	0.0 (fixed)	57.2 ± 4.2	36.9σ
$\Sigma(1385)^+\pi^0$	0.43 ± 0.06	-0.23 ± 0.18	7.18 ± 0.60	14.8σ
$\Sigma(1385)^0\pi^+$	0.37 ± 0.07	2.84 ± 0.23	7.92 ± 0.72	16.0σ
$\Sigma(1670)^+\pi^0$	0.31 ± 0.08	-0.77 ± 0.23	2.90 ± 0.63	5.1σ
$\Sigma(1670)^0\pi^+$	0.41 ± 0.07	2.77 ± 0.20	2.65 ± 0.58	5.2σ
$\Sigma(1750)^+\pi^0$	1.75 ± 0.21	-1.73 ± 0.11	16.6 ± 2.2	10.1σ
$\Sigma(1750)^0\pi^+$	1.83 ± 0.21	1.34 ± 0.11	17.5 ± 2.3	10.2σ
$\Lambda + NR_{1-}$	4.05 ± 0.47	2.16 ± 0.13	29.7 ± 4.5	10.5σ

Table 4. Numerical results of the total amplitudes for different components in the nominal fit, along with the FFs and the corresponding significance. The total FF is 141.8%. Only statistical uncertainties are listed.

The statistical uncertainties for FFs are obtained with the standard form of error propagation. Let Y be the variable whose error needs to be calculated, \mathbf{X} the variables with a corresponding error matrix V_{ij} in eq. (4.20) and $\boldsymbol{\mu}$ the nominal results of the floating variables \mathbf{X} , the squared uncertainty of Y is estimated as

$$\sigma_Y^2 = \sum_{ij} \left(\frac{\partial Y}{\partial X_i} \right)_{\mathbf{X}=\boldsymbol{\mu}} \cdot V_{ij} \cdot \left(\frac{\partial Y}{\partial X_j} \right)_{\mathbf{X}=\boldsymbol{\mu}}. \quad (4.23)$$

4.4 Nominal fit results

The starting point in the construction of the nominal fit hypothesis of the PWA is the inclusion of the main resonances involved in the decay, i.e. $\Sigma(1385)^+$, $\Sigma(1385)^0$ and $\rho(770)^+$. The $\rho(770)^+$ component is chosen as the reference channel due to its dominant contribution, and the magnitude and phase of its total amplitude are fixed to one and zero, respectively.

In addition, the statistical significance of the contribution from excited Σ states is evaluated, including $\Sigma(1660)$, $\Sigma(1670)$, $\Sigma(1750)$, $\Sigma(1775)$, $\Sigma(1910)$, $\Sigma(1915)$, and $\Sigma(2030)$ (considered as established by the PDG [11] with a score of at least four stars), as well as from the \mathcal{S} -wave (NR_{0+}), \mathcal{P} -wave (NR_{1-}), and \mathcal{D} -wave (NR_{2+}) non-resonant components in the $M_{\pi^+\pi^0}$ spectrum, based on the change of the NLL value when including singly each of these components. The statistical significance is calculated from the change of the NLL values with and without including the component, by taking into account the change of the number of degrees of freedom. The results show that the resonances $\Sigma(1670)$ and $\Sigma(1750)$, along with the non-resonant components NR_{1-} , have statistical significance larger than 5σ , while none of the other tested contributions exceeds this threshold.

Therefore, the nominal components are determined to be the $\rho(770)^+$, $\Sigma(1385)^+$, $\Sigma(1385)^0$, $\Sigma(1670)^+$, $\Sigma(1670)^0$, $\Sigma(1750)^+$, and $\Sigma(1750)^0$ states, as well as the NR_{1-} component, whose statistical significances are listed in table 4. The mass and width parameters of the $\rho(770)^+$, $\Sigma(1385)^+$, and $\Sigma(1385)^0$ states are fixed to the corresponding world average values [11], while the resonance parameters of the other Σ^* resonances are taken

$\frac{1}{2}^+(\Lambda_c^+) \rightarrow \frac{3}{2}^+(\Sigma(1385)^+) + 0^-(\pi^0)$			$\frac{1}{2}^+(\Lambda_c^+) \rightarrow \frac{3}{2}^+(\Sigma(1385)^0) + 0^-(\pi^+)$		
Amplitude	Magnitude	Phase ϕ (rad)	Amplitude	Magnitude	Phase ϕ (rad)
$g_{1,\frac{3}{2}}^{\Sigma(1385)^+}$	1.0 (fixed)	0.0 (fixed)	$g_{1,\frac{3}{2}}^{\Sigma(1385)^0}$	1.0 (fixed)	0.0 (fixed)
$g_{2,\frac{3}{2}}^{\Sigma(1385)^+}$	1.29 ± 0.25	2.82 ± 0.18	$g_{2,\frac{3}{2}}^{\Sigma(1385)^0}$	1.70 ± 0.38	2.70 ± 0.22
$\frac{1}{2}^+(\Lambda_c^+) \rightarrow \frac{3}{2}^-(\Sigma(1670)^+) + 0^-(\pi^0)$			$\frac{1}{2}^+(\Lambda_c^+) \rightarrow \frac{3}{2}^-(\Sigma(1670)^0) + 0^-(\pi^+)$		
Amplitude	Magnitude	Phase ϕ (rad)	Amplitude	Magnitude	Phase ϕ (rad)
$g_{1,\frac{3}{2}}^{\Sigma(1670)^+}$	1.0 (fixed)	0.0 (fixed)	$g_{1,\frac{3}{2}}^{\Sigma(1670)^0}$	1.0 (fixed)	0.0 (fixed)
$g_{2,\frac{3}{2}}^{\Sigma(1670)^+}$	1.39 ± 0.42	0.85 ± 0.26	$g_{2,\frac{3}{2}}^{\Sigma(1670)^0}$	0.74 ± 0.18	0.29 ± 0.24
$\frac{1}{2}^+(\Lambda_c^+) \rightarrow \frac{1}{2}^-(\Sigma(1750)^+) + 0^-(\pi^0)$			$\frac{1}{2}^+(\Lambda_c^+) \rightarrow \frac{1}{2}^-(\Sigma(1750)^0) + 0^-(\pi^+)$		
Amplitude	Magnitude	Phase ϕ (rad)	Amplitude	Magnitude	Phase ϕ (rad)
$g_{0,\frac{1}{2}}^{\Sigma(1750)^+}$	1.0 (fixed)	0.0 (fixed)	$g_{0,\frac{1}{2}}^{\Sigma(1750)^0}$	1.0 (fixed)	0.0 (fixed)
$g_{1,\frac{1}{2}}^{\Sigma(1750)^+}$	0.45 ± 0.10	-2.28 ± 0.22	$g_{1,\frac{1}{2}}^{\Sigma(1750)^0}$	0.38 ± 0.10	-2.03 ± 0.20
$\frac{1}{2}^+(\Lambda_c^+) \rightarrow \frac{1}{2}^+(\Lambda) + 1^-(\rho(770)^+)$			$\frac{1}{2}^+(\Lambda_c^+) \rightarrow \frac{1}{2}^+(\Lambda) + 1^-(NR_{1-})$		
Amplitude	Magnitude	Phase ϕ (rad)	Amplitude	Magnitude	Phase ϕ (rad)
$g_{0,\frac{1}{2}}^\rho$	1.0 (fixed)	0.0 (fixed)	$g_{0,\frac{1}{2}}^{NR}$	1.0 (fixed)	0.0 (fixed)
$g_{1,\frac{1}{2}}^\rho$	0.48 ± 0.12	-1.69 ± 0.12	$g_{1,\frac{1}{2}}^{NR}$	0.94 ± 0.12	-0.49 ± 0.16
$g_{1,\frac{3}{2}}^\rho$	0.90 ± 0.10	0.48 ± 0.13	$g_{1,\frac{3}{2}}^{NR}$	0.21 ± 0.09	-2.84 ± 0.53
$g_{2,\frac{3}{2}}^\rho$	0.55 ± 0.08	-0.04 ± 0.18	$g_{2,\frac{3}{2}}^{NR}$	0.33 ± 0.14	-1.92 ± 0.30
$\frac{1}{2}^+(\Lambda) \rightarrow \frac{1}{2}^+(p) + 0^-(\pi^-)$					
Amplitude	Magnitude	Phase ϕ (rad)			
$g_{0,\frac{1}{2}}^\Lambda$	1.0 (fixed)	0.0 (fixed)			
$g_{1,\frac{1}{2}}^\Lambda$	0.435376 (fixed)	0.0 (fixed)			

Table 5. Numerical results of the partial wave amplitudes g_{ls} for different resonances in the nominal fit. Only statistical uncertainties are listed.

from the most recent measurements [53]. Moreover, the Λ decay asymmetry parameter $\alpha_\Lambda = 0.732 \pm 0.014$ [11, 54–56] is used, as discussed in section 4.5.

The constructed NLL of the nominal fit contains 38 floating parameters in total, consisting of magnitudes and phases of the total amplitudes (14) and partial wave amplitudes (24), whose fit results are listed in table 4 and table 5. The fractions of the interference

I.F.	$\Lambda + NR_{1-}$	$\Sigma(1385)^0\pi^+$	$\Sigma(1385)^+\pi^0$	$\Sigma(1670)^0\pi^+$	$\Sigma(1670)^+\pi^0$	$\Sigma(1750)^0\pi^+$	$\Sigma(1750)^+\pi^0$
$\Sigma(1385)^0\pi^+$	-0.50 ± 0.38						
$\Sigma(1385)^+\pi^0$	-0.76 ± 0.36	-0.05 ± 0.04					
$\Sigma(1670)^0\pi^+$	-0.36 ± 0.17	-0.00 ± 0.00	-0.66 ± 0.09				
$\Sigma(1670)^+\pi^0$	-0.34 ± 0.15	-0.58 ± 0.12	0.00 ± 0.00	0.04 ± 0.02			
$\Sigma(1750)^0\pi^+$	-8.1 ± 3.1	-0.03 ± 0.00	0.43 ± 0.07	-0.01 ± 0.00	0.08 ± 0.05		
$\Sigma(1750)^+\pi^0$	-7.2 ± 3.1	0.35 ± 0.08	-0.02 ± 0.00	0.23 ± 0.05	-0.00 ± 0.00	-6.23 ± 0.92	
$\Lambda\rho(770)^+$	-2.7 ± 4.4	-5.94 ± 0.56	-6.01 ± 0.46	0.72 ± 0.29	1.29 ± 0.26	-2.1 ± 1.3	-3.1 ± 1.3

Table 6. Interference fractions (I.F.) between Λ_c^+ amplitudes in units of percentage. The uncertainties are statistical only.

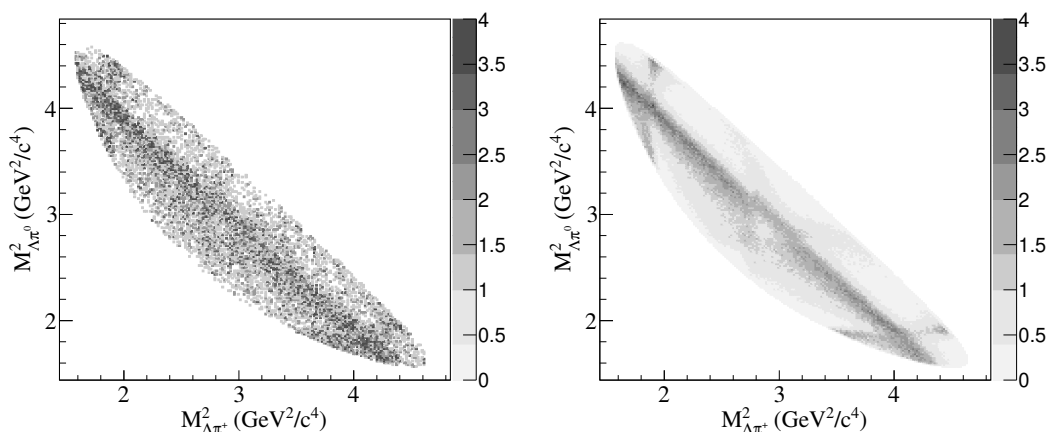


Figure 5. The Dalitz plot distributions of data (left) and fit results (right).

parts can be found in table 6. The Dalitz plot distributions of data and fit results are shown in figure 5, and other one-dimensional projections are shown in figures 6 and 7. Using the FFs listed in table 4 multiplied by the total three-body BF $\mathcal{B}(\Lambda_c^+ \rightarrow \Lambda\pi^+\pi^0) = (7.1 \pm 0.4)\%$ [10, 11] and considering the intermediate BF $\mathcal{B}(\Sigma(1385) \rightarrow \Lambda\pi)$, the absolute BFs of the involved resonances are obtained as listed in table 7. For the resonances $\rho(770)^+$ and $\Sigma(1385)$, further studies on the decay asymmetries and the relevant systematic uncertainties are performed, in order to better confront them with the theoretical calculations.

4.5 Decay asymmetry parameters

The decay asymmetry parameters α are related to the interference effects among the different partial waves, and the corresponding expressions are considered in the formula of the partial wave amplitudes. When the intermediate state is at its nominal mass, the helicity amplitude of a two-body decay can be written under LS coupling expansion [48] as

$$H_{\lambda_1, \lambda_2} = \sum_{ls} g_{ls} \sqrt{\frac{2l+1}{2J_0+1}} \langle l0, s\delta | J_0, \delta \rangle \langle J_1 J_2, \lambda_1 - \lambda_2 | s, \delta \rangle, \quad (4.24)$$

where g_{ls} is the partial wave amplitude.

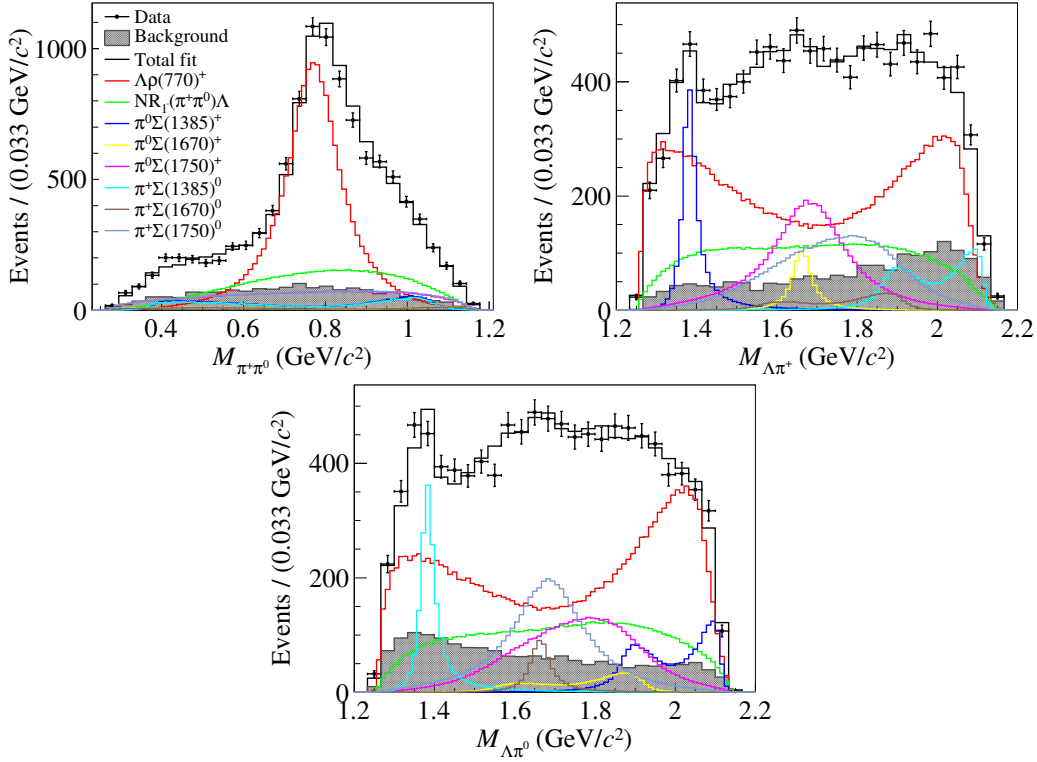


Figure 6. Projections of the fit results in the invariant mass spectra $M_{\pi^+\pi^0}$, $M_{\Lambda\pi^+}$ and $M_{\Lambda\pi^0}$. Points with error bars denote data. Different styles of the curves denote different components.

	Result
$\frac{\mathcal{B}(\Lambda_c^+ \rightarrow \Lambda\rho(770)^+)}{\mathcal{B}(\Lambda_c^+ \rightarrow \Lambda\pi^+\pi^0)}$	$(57.2 \pm 4.2 \pm 4.9)\%$
$\frac{\mathcal{B}(\Lambda_c^+ \rightarrow \Sigma(1385)^+\pi^0) \cdot \mathcal{B}(\Sigma(1385)^+ \rightarrow \Lambda\pi^+)}{\mathcal{B}(\Lambda_c^+ \rightarrow \Lambda\pi^+\pi^0)}$	$(7.18 \pm 0.60 \pm 0.64)\%$
$\frac{\mathcal{B}(\Lambda_c^+ \rightarrow \Sigma(1385)^0\pi^+) \cdot \mathcal{B}(\Sigma(1385)^0 \rightarrow \Lambda\pi^0)}{\mathcal{B}(\Lambda_c^+ \rightarrow \Lambda\pi^+\pi^0)}$	$(7.92 \pm 0.72 \pm 0.80)\%$
$\mathcal{B}(\Lambda_c^+ \rightarrow \Lambda\rho(770)^+)$	$(4.06 \pm 0.30 \pm 0.35 \pm 0.23) \times 10^{-2}$
$\mathcal{B}(\Lambda_c^+ \rightarrow \Sigma(1385)^+\pi^0)$	$(5.86 \pm 0.49 \pm 0.52 \pm 0.35) \times 10^{-3}$
$\mathcal{B}(\Lambda_c^+ \rightarrow \Sigma(1385)^0\pi^+)$	$(6.47 \pm 0.59 \pm 0.66 \pm 0.38) \times 10^{-3}$
$\alpha_{\Lambda\rho(770)^+}$	$-0.763 \pm 0.053 \pm 0.045$
$\alpha_{\Sigma(1385)^+\pi^0}$	$-0.917 \pm 0.069 \pm 0.056$
$\alpha_{\Sigma(1385)^0\pi^+}$	$-0.789 \pm 0.098 \pm 0.056$

Table 7. Numerical results of the BFs and decay asymmetry parameters, where the first uncertainties are statistical and the second systematic. For the absolute BFs, the third uncertainties are due to the quoted external BFs $\mathcal{B}(\Lambda_c^+ \rightarrow \Lambda\pi^+\pi^0)$ and $\mathcal{B}(\Sigma(1385) \rightarrow \Lambda\pi)$. The relative BFs are equivalent to the FFs listed in table 4.

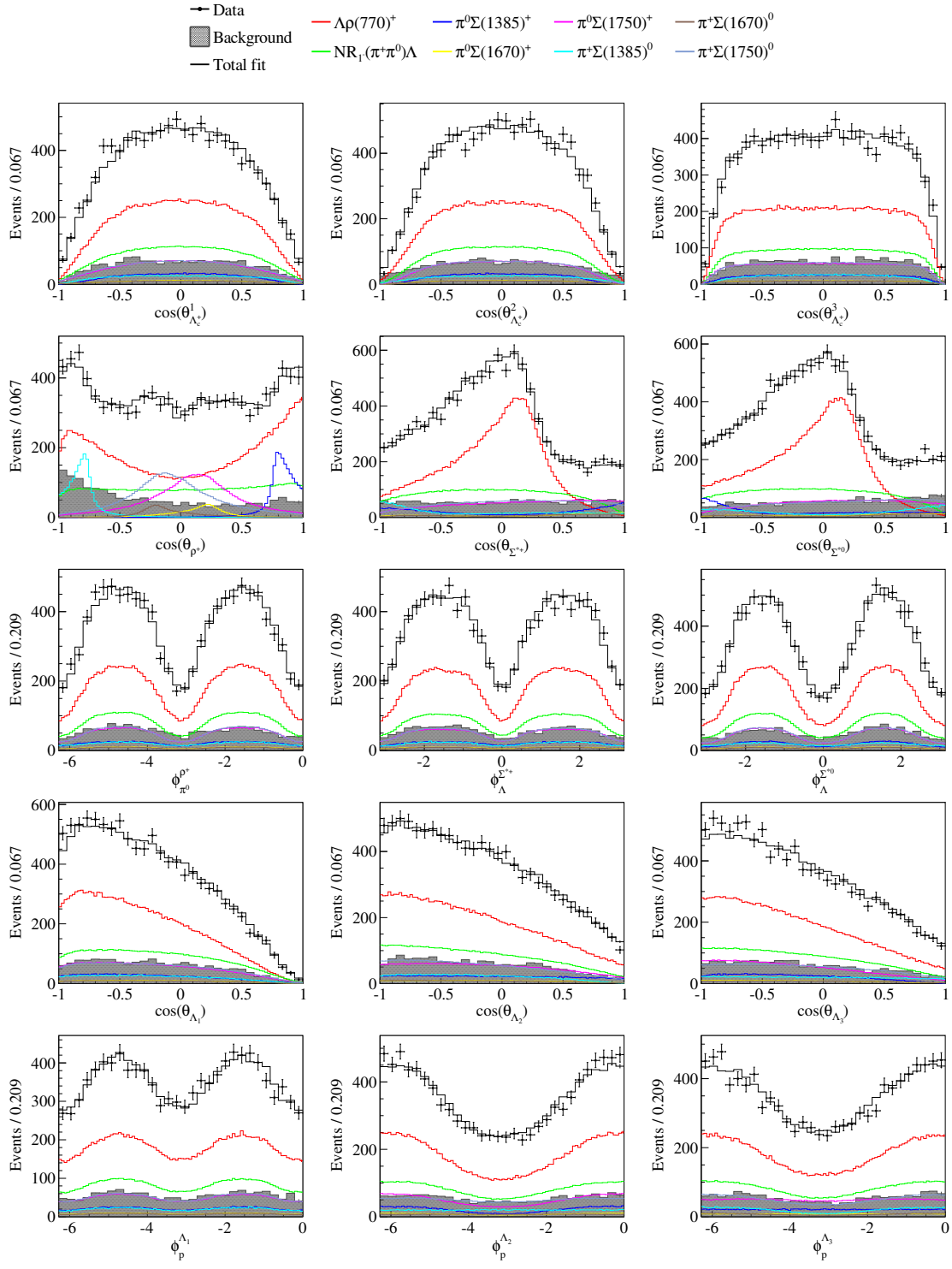


Figure 7. Projections of the fit results in the distributions of helicity angles.

When considering the decay $\Lambda \rightarrow p\pi^-$, the two helicity amplitudes are obtained as

$$H_{0,\pm\frac{1}{2}}^\Lambda = \frac{\left(g_{0,\frac{1}{2}}^\Lambda \pm g_{1,\frac{1}{2}}^\Lambda\right)}{\sqrt{2}}, \quad (4.25)$$

and the Λ decay asymmetry parameter α_Λ is expressed as

$$\alpha_\Lambda = \frac{|H_{0,\frac{1}{2}}^\Lambda|^2 - |H_{0,-\frac{1}{2}}^\Lambda|^2}{|H_{0,\frac{1}{2}}^\Lambda|^2 + |H_{0,-\frac{1}{2}}^\Lambda|^2} = \frac{2\Re\left(g_{0,\frac{1}{2}}^\Lambda \cdot \bar{g}_{1,\frac{1}{2}}^\Lambda\right)}{|g_{0,\frac{1}{2}}^\Lambda|^2 + |g_{1,\frac{1}{2}}^\Lambda|^2}, \quad (4.26)$$

which represents the interference between the \mathcal{S} and \mathcal{P} partial wave amplitudes. In eq. (4.16), the helicity of the proton $\lambda_p = -1/2$ and $\lambda_p = 1/2$ is summed directly outside the module square. This reduces the relative partial wave amplitude $g_{1,\frac{1}{2}}^\Lambda/g_{0,\frac{1}{2}}^\Lambda$ by one degree, by fixing the phase of $g_{1,\frac{1}{2}}^\Lambda$ to zero and the magnitude to the value listed in table 5 according to eq. (4.26) with the input value $\alpha_\Lambda = 0.732 \pm 0.014$.

The decay $\Lambda_c^+ \rightarrow \Lambda\rho(770)^+$ is described by four helicity amplitudes and the differential decay width depends on the decay asymmetry $\alpha_{\Lambda\rho(770)^+}$ [57]

$$\frac{d\Gamma}{d\cos\Theta_\Lambda} \propto 1 + \alpha_{\Lambda\rho(770)^+} \cdot \alpha_\Lambda \cdot \cos\Theta_\Lambda, \quad (4.27)$$

where Θ_Λ is the Λ helicity angle, denoted as θ_{Λ_1} in figure 4. Using eq. (4.24), the four helicity amplitudes are denoted as

$$\begin{aligned} H_{-\frac{1}{2},-1}^\rho &= -\frac{g_{0,\frac{1}{2}}^\rho}{\sqrt{3}} + \frac{g_{1,\frac{1}{2}}^\rho}{\sqrt{3}} - \frac{g_{1,\frac{3}{2}}^\rho}{\sqrt{6}} + \frac{g_{2,\frac{3}{2}}^\rho}{\sqrt{6}}, \\ H_{-\frac{1}{2},0}^\rho &= -\frac{g_{0,\frac{1}{2}}^\rho}{\sqrt{6}} - \frac{g_{1,\frac{1}{2}}^\rho}{\sqrt{6}} - \frac{g_{1,\frac{3}{2}}^\rho}{\sqrt{3}} - \frac{g_{2,\frac{3}{2}}^\rho}{\sqrt{3}}, \\ H_{\frac{1}{2},0}^\rho &= \frac{g_{0,\frac{1}{2}}^\rho}{\sqrt{6}} - \frac{g_{1,\frac{1}{2}}^\rho}{\sqrt{6}} - \frac{g_{1,\frac{3}{2}}^\rho}{\sqrt{3}} + \frac{g_{2,\frac{3}{2}}^\rho}{\sqrt{3}}, \\ H_{\frac{1}{2},1}^\rho &= \frac{g_{0,\frac{1}{2}}^\rho}{\sqrt{3}} + \frac{g_{1,\frac{1}{2}}^\rho}{\sqrt{3}} - \frac{g_{1,\frac{3}{2}}^\rho}{\sqrt{6}} - \frac{g_{2,\frac{3}{2}}^\rho}{\sqrt{6}}. \end{aligned} \quad (4.28)$$

The decay asymmetry $\alpha_{\Lambda\rho(770)^+}$ can be expressed with the partial wave amplitudes as

$$\begin{aligned} \alpha_{\Lambda\rho(770)^+} &= \frac{|H_{\frac{1}{2},1}^\rho|^2 - |H_{-\frac{1}{2},-1}^\rho|^2 + |H_{\frac{1}{2},0}^\rho|^2 - |H_{-\frac{1}{2},0}^\rho|^2}{|H_{\frac{1}{2},1}^\rho|^2 + |H_{-\frac{1}{2},-1}^\rho|^2 + |H_{\frac{1}{2},0}^\rho|^2 + |H_{-\frac{1}{2},0}^\rho|^2} \\ &= \frac{\sqrt{\frac{1}{9}} \cdot 2 \cdot \Re\left(g_{0,\frac{1}{2}}^\rho \cdot \bar{g}_{1,\frac{1}{2}}^\rho - g_{1,\frac{3}{2}}^\rho \cdot \bar{g}_{2,\frac{3}{2}}^\rho\right) - \sqrt{\frac{8}{9}} \cdot 2 \cdot \Re\left(g_{0,\frac{1}{2}}^\rho \cdot \bar{g}_{1,\frac{3}{2}}^\rho + g_{1,\frac{1}{2}}^\rho \cdot \bar{g}_{2,\frac{3}{2}}^\rho\right)}{|g_{0,\frac{1}{2}}^\rho|^2 + |g_{1,\frac{1}{2}}^\rho|^2 + |g_{1,\frac{3}{2}}^\rho|^2 + |g_{2,\frac{3}{2}}^\rho|^2}. \end{aligned} \quad (4.29)$$

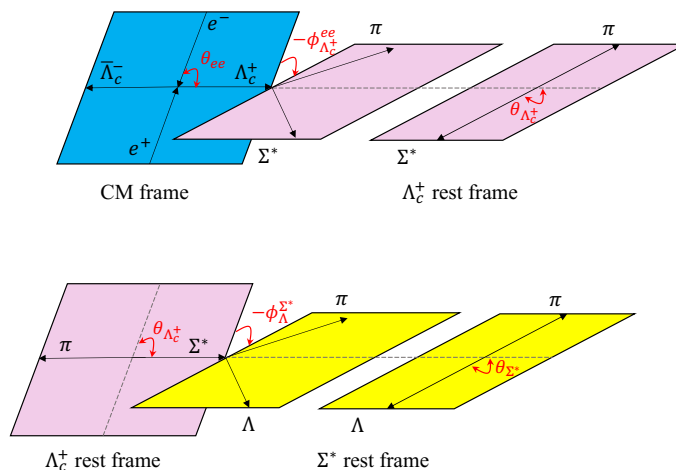


Figure 8. Definitions of helicity angles for the cascade process $e^+e^- \rightarrow \Lambda_c^+\bar{\Lambda}_c^-$, $\Lambda_c^+ \rightarrow \Sigma^*\pi$, $\Sigma^* \rightarrow \Lambda\pi$, where Σ^* denotes $\Sigma(1385)^+$ or $\Sigma(1385)^0$. The convention of the notation is the same with figure 4.

For the process $\Lambda_c^+ \rightarrow \Sigma(1385)\pi$, the corresponding decay asymmetry appears in the differential width expression [27]

$$\frac{d\Gamma}{d\cos\theta_{ee}d\cos\theta_{\Lambda_c^+}d\cos\theta_{\Sigma^*\pi}d\phi_{\Lambda_c^+}^{ee}} \propto (7 + 9\cos(2\theta_{\Sigma^*})) \cdot \left(1 + \alpha_0\cos^2(\theta_{ee}) + \alpha_{\Sigma^*\pi}\sqrt{1 - \alpha_0^2}\sin\Delta_0\cos\theta_{ee}\sin\theta_{ee}\sin\theta_{\Lambda_c^+}\sin\phi_{\Lambda_c^+}^{ee}\right), \quad (4.30)$$

where α_0 and Δ_0 are constants related to the $\Lambda_c^+\bar{\Lambda}_c^-$ production, and the definitions of the individual helicity angles can be found in figure 8. There are two different helicity amplitudes in this process, which can be written using eq. (4.24) as

$$H_{0,\pm\frac{1}{2}}^{\Sigma(1385)} = \mp \frac{\left(g_{2,\frac{3}{2}}^{\Sigma(1385)} \pm g_{1,\frac{3}{2}}^{\Sigma(1385)}\right)}{\sqrt{2}}. \quad (4.31)$$

Thus, the decay asymmetry $\alpha_{\Sigma(1385)\pi}$ can be expressed with the partial wave amplitudes as

$$\alpha_{\Sigma(1385)\pi} = \frac{|H_{0,\frac{1}{2}}^{\Sigma(1385)}|^2 - |H_{0,-\frac{1}{2}}^{\Sigma(1385)}|^2}{|H_{0,\frac{1}{2}}^{\Sigma(1385)}|^2 + |H_{0,-\frac{1}{2}}^{\Sigma(1385)}|^2} = \frac{2\Re\left(g_{1,\frac{3}{2}}^{\Sigma(1385)} \cdot \bar{g}_{2,\frac{3}{2}}^{\Sigma(1385)}\right)}{|g_{1,\frac{3}{2}}^{\Sigma(1385)}|^2 + |g_{2,\frac{3}{2}}^{\Sigma(1385)}|^2}. \quad (4.32)$$

Through the nominal fit results of the partial wave amplitudes listed in table 5, the decay asymmetry parameters can be obtained, as listed in table 7. The statistical uncertainties of the asymmetry parameters are calculated via error propagation in eq. (4.23).

	FF $_{\rho(770)^+}$	FF $_{\Sigma(1385)^+}$	FF $_{\Sigma(1385)^0}$	$\alpha_{\Lambda\rho(770)^+}$	$\alpha_{\Sigma(1385)^+\pi^0}$	$\alpha_{\Sigma(1385)^0\pi^+}$
I	0.47	0.32	0.62	0.15	0.18	0.32
II	0.15	0.14	0.15	0.16	0.01	0.01
III	0.88	0.39	0.36	0.50	0.07	0.29
IV	0.11	0.41	0.26	0.21	0.22	0.21
V	0.06	0.25	0.43	0.03	0.07	0.03
VI	0.49	0.79	0.65	0.57	0.74	0.20
VII	0.08	0.13	0.01	0.20	0.16	0.23
VIII	0.20	0.10	0.13	0.08	0.06	0.04
Total	1.15	1.08	1.11	0.84	0.81	0.57

Table 8. Systematic uncertainties (in units of corresponding statistical uncertainties) on the FFs of $\Sigma(1385)^+$, $\Sigma(1385)^0$ and $\rho(770)^+$, and the corresponding decay asymmetry parameters $\alpha_{\Lambda\rho(770)^+}$, $\alpha_{\Sigma(1385)^+\pi^0}$ and $\alpha_{\Sigma(1385)^0\pi^+}$. The total systematic uncertainties are obtained by summing up all contributions in quadrature.

5 Systematic uncertainties

The systematic uncertainties of the observables, including the FFs of the components $\rho(770)^+$, $\Sigma(1385)^+$, and $\Sigma(1385)^0$, as well as their decay asymmetry parameters $\alpha_{\Lambda\rho(770)^+}$, $\alpha_{\Sigma(1385)^+\pi^0}$, and $\alpha_{\Sigma(1385)^0\pi^+}$, are estimated. In general, the following sources are considered: (I) fixed parameters, (II) mass dependent width, (III) radius parameter, (IV) background description, (V) data-MC differences, (VI) resonance components, (VII) polarization of the initial Λ_c^+ , and (VIII) fit bias. All the systematic uncertainties are listed in table 8.

- I. *Fixed parameters.* In the nominal fit, the mass and width parameters of resonances and the Λ decay asymmetry parameter are fixed according to refs. [11, 53–56]. To estimate the relevant systematic uncertainties, the fixed parameters are varied within $\pm 1\sigma$ and the fit procedure is repeated. The quadratic sums of the largest variations from each parameter are assigned as systematic uncertainties.
- II. *Mass dependent width.* In the nominal fit, the running width is used as in eq. (4.9) to describe the width of a resonance. To estimate the potential systematic uncertainties, an alternative method using a pseudo coupled channel approach is considered, where the full width consists of partial widths from the main decay channels $N\bar{K}$, $\Sigma\pi$, and $\Lambda\pi$, as described in refs. [53, 58]. Using the coupled channel widths, the fit procedure is repeated, and the resulting variations are assigned as systematic uncertainties.
- III. *Radius parameter.* In the nominal fit, the radius parameter d is chosen as $d = 0.73$ fm [50]. To estimate the potential bias, the fits are performed by setting d at the alternative values derived from ref. [50], $d = 0.53$ fm and $d = 1.16$ fm, and the largest variations are assigned as systematic uncertainties.

IV. *Background description.* The systematic uncertainties arising from the background description originate from two sources: background fractions and background shape.

In the nominal fit, the background fractions are fixed according to the fit results given in table 3. To estimate systematic uncertainties, the background fraction for each energy point is varied within $\pm 1\sigma$, and the fit procedure is repeated. The quadratic sums of the largest variations from each fraction are assigned as the associated systematic uncertainties.

For the background shape, the M_{BC} sideband is used to describe the background components in the M_{BC} signal region. To understand the possible bias coming from the background modelling based on sideband data, this approach is tested on a large toy MC sample generated according to the fitted amplitudes in the nominal fit plus the background processes in the inclusive MC samples. The PWA fit is applied to the toy sample and the variations of the output fit results from the input amplitudes are assigned as systematic uncertainties.

Finally, the systematic uncertainties arising from background description are assigned as quadratic sums of the above two sources.

V. *Data-MC differences.* To estimate possible systematic uncertainties due to the difference between the MC-determined efficiency and the experimental one, the effects from tracking and PID of π^+ candidates, and the reconstruction of Λ and π^0 candidates are considered. The reconstruction efficiency differences between data and MC simulations have been investigated in previous studies, such as Λ reconstruction in ref. [59], π^0 reconstruction in ref. [60], and π^+ tracking and PID in ref. [61]. The correction factors $w = \varepsilon_{\text{Data}}/\varepsilon_{\text{MC}}$ are assigned as the weighting factors of the PHSP MC sample and the fit procedure is repeated. Including the weighting factors, eq. (4.17) becomes

$$\int |\mathcal{A}|^2 d\Phi \propto \frac{1}{\sum_{i \in \text{PHSP}} w(x_i)} \sum_{i \in \text{PHSP}} w(x_i) \cdot |\mathcal{A}(x_i)|^2, \quad (5.1)$$

where $w(x_i)$ is the weighting factor for the i -th event. The resulting variations on the final results are considered as systematic uncertainties.

VI. *Resonance components.* To estimate the systematic uncertainties from resonance components, the amplitude fit is repeated by including each possible additional resonance among those listed in section 4.4. The corresponding largest changes on the fit results among all variations of resonance components are taken into account as systematic uncertainties.

VII. *Polarization of initial Λ_c^+ .* In the nominal fit, the total amplitude is constructed using eq. (4.16), where the initial state Λ_c^+ is assumed to be unpolarized. To estimate the systematic uncertainties due to polarization of initial Λ_c^+ , the polarization parameters

$P_{x,y,z}$ are introduced as free parameters, and the total amplitude is rewritten as

$$|\mathcal{A}'|^2 = \sum_{\lambda_p} \left[\left(\mathcal{A}_{-\frac{1}{2},\lambda_p} \mathcal{A}_{\frac{1}{2},\lambda_p} \right) \cdot \frac{1}{2} \cdot \begin{pmatrix} 1 + P_z & P_x - iP_y \\ P_x + iP_y & 1 - P_z \end{pmatrix} \cdot \begin{pmatrix} \mathcal{A}_{-\frac{1}{2},\lambda_p}^* \\ \mathcal{A}_{\frac{1}{2},\lambda_p}^* \end{pmatrix} \right]. \quad (5.2)$$

Here, the polarization parameters indicate the average polarization of a single Λ_c^+ . Then, using the alternative total amplitude, the fit procedure is repeated, and the corresponding variations are assigned as systematic uncertainties.

VIII. *Fit bias.* To estimate the potential fit bias effect, an input-output check is performed. Several toy MC samples are generated, where the signal events are generated according to the results of the nominal fit, and the background events are generated using a bootstrap method [62]. The PWA fit is performed to each toy sample and the pull distributions for every fitted variable are plotted. The mean values of the pull distributions, which indicate a possible fit bias, are considered as systematic uncertainties.

The total systematic uncertainty is obtained by summing up all contributions in quadrature, as listed in table 7. The systematic uncertainties of the BFs are of a similar size as the corresponding statistical uncertainties, while the systematic uncertainties for the decay asymmetry parameters are rather smaller.

6 Summary

To summarize, based on the e^+e^- collision samples corresponding to an integrated luminosity of 4.4 fb^{-1} collected with the BESIII detector at c.m. energies between 4.6 GeV and 4.7 GeV, the first PWA of the charmed baryon hadronic decay $\Lambda_c^+ \rightarrow \Lambda\pi^+\pi^0$ is performed. Based on the analysis results, the relative BFs for the resonant components are measured to be

$$\begin{aligned} \frac{\mathcal{B}(\Lambda_c^+ \rightarrow \Lambda\rho(770)^+)}{\mathcal{B}(\Lambda_c^+ \rightarrow \Lambda\pi^+\pi^0)} &= (57.2 \pm 4.2 \pm 4.9)\%, \\ \frac{\mathcal{B}(\Lambda_c^+ \rightarrow \Sigma(1385)^+\pi^0) \cdot \mathcal{B}(\Sigma(1385)^+ \rightarrow \Lambda\pi^+)}{\mathcal{B}(\Lambda_c^+ \rightarrow \Lambda\pi^+\pi^0)} &= (7.18 \pm 0.60 \pm 0.64)\%, \\ \frac{\mathcal{B}(\Lambda_c^+ \rightarrow \Sigma(1385)^0\pi^+) \cdot \mathcal{B}(\Sigma(1385)^0 \rightarrow \Lambda\pi^0)}{\mathcal{B}(\Lambda_c^+ \rightarrow \Lambda\pi^+\pi^0)} &= (7.92 \pm 0.72 \pm 0.80)\%. \end{aligned}$$

Here, the first uncertainty is statistical and the second is systematic. After taking into account $\mathcal{B}(\Lambda_c^+ \rightarrow \Lambda\pi^+\pi^0) = (7.1 \pm 0.4)\%$ and $\mathcal{B}(\Sigma(1385) \rightarrow \Lambda\pi) = (87.5 \pm 1.5)\%$ [11], the absolute BFs are obtained for the first time:

$$\begin{aligned} \mathcal{B}(\Lambda_c^+ \rightarrow \Lambda\rho(770)^+) &= (4.06 \pm 0.30 \pm 0.35 \pm 0.23)\%, \\ \mathcal{B}(\Lambda_c^+ \rightarrow \Sigma(1385)^+\pi^0) &= (5.86 \pm 0.49 \pm 0.52 \pm 0.35) \times 10^{-3}, \\ \mathcal{B}(\Lambda_c^+ \rightarrow \Sigma(1385)^0\pi^+) &= (6.47 \pm 0.59 \pm 0.66 \pm 0.38) \times 10^{-3}, \end{aligned}$$

	Theoretical calculation		This work	PDG
$10^2 \times \mathcal{B}(\Lambda_c^+ \rightarrow \Lambda\rho(770)^+)$	4.81 ± 0.58 [13]	4.0 [14, 15]	4.06 ± 0.52	< 6
$10^3 \times \mathcal{B}(\Lambda_c^+ \rightarrow \Sigma(1385)^+\pi^0)$	2.8 ± 0.4 [16]	2.2 ± 0.4 [17]	5.86 ± 0.80	—
$10^3 \times \mathcal{B}(\Lambda_c^+ \rightarrow \Sigma(1385)^0\pi^+)$	2.8 ± 0.4 [16]	2.2 ± 0.4 [17]	6.47 ± 0.96	—
$\alpha_{\Lambda\rho(770)^+}$	-0.27 ± 0.04 [13]	-0.32 [14, 15]	-0.763 ± 0.070	—
$\alpha_{\Sigma(1385)^+\pi^0}$		$-0.91_{-0.10}^{+0.45}$ [17]	-0.917 ± 0.089	—
$\alpha_{\Sigma(1385)^0\pi^+}$		$-0.91_{-0.10}^{+0.45}$ [17]	-0.79 ± 0.11	—

Table 9. The comparison among this work, various theoretical calculations and PDG results. Here, the uncertainties of this work are the combined uncertainties. “—” means unavailable.

where the third uncertainty is due to the input $\mathcal{B}(\Lambda_c^+ \rightarrow \Lambda\pi^+\pi^0)$ and $\mathcal{B}(\Sigma(1385) \rightarrow \Lambda\pi)$. Based on the results of the PWA, the decay asymmetry parameters for the resonant components are determined for the first time:

$$\begin{aligned} \alpha_{\Lambda\rho(770)^+} &= -0.763 \pm 0.053 \pm 0.045, \\ \alpha_{\Sigma(1385)^+\pi^0} &= -0.917 \pm 0.069 \pm 0.056, \\ \alpha_{\Sigma(1385)^0\pi^+} &= -0.789 \pm 0.098 \pm 0.056. \end{aligned}$$

The comparison between this work and various theoretical calculations can be found in table 9. The $\Lambda_c^+ \rightarrow \Lambda\rho(770)^+$ BF presented in this paper has good agreement with the theoretical predictions evaluated in refs. [13–15]. However, the corresponding asymmetry parameter differs significantly with their calculations. The comparison of the measurements presented here with the prediction of refs. [16, 17] for the decays $\Lambda_c^+ \rightarrow \Sigma(1385)^{+(0)}\pi^{0(+)}$ presents an opposite situation; the asymmetry parameters are in good agreement, but a more than 3σ difference is observed between the BF values. As none of the theoretical models is able to explain both the BFs and the decay asymmetries, the results reported in this paper provide a crucial input to improve and extend the current understanding of the dynamics of the charmed baryon hadronic decays.

A Alignment angle calculation

In the helicity formalism, several alignment angles are used in constructing the full amplitude as expressed in eq. (4.15). Here, we detail the calculations of the alignment angles. The alignment angle is the correction of different definition of z -axis in helicity amplitude. Suppose an arbitrary decay $0 \rightarrow 1 + 2$, of which the helicity formula can be expressed as

$$\langle p_1, \lambda_1; p_2, \lambda_2 | U | p_0, \lambda_0 \rangle = H_{\lambda_1, \lambda_2} D_{\lambda_0, \lambda_1 - \lambda_2}^{J_0^*}(\phi, \theta, 0), \quad (\text{A.1})$$

where $p_{0,1,2}$ are momenta, and $\lambda_{0,1,2}$ are helicities for the particles. This means the evolution operator U can be divided into two parts, the rotation part R

$$\langle p_0, \lambda_1 - \lambda_2 | R(\phi, \theta, 0) | p_0, \lambda_0 \rangle = D_{\lambda_0, \lambda_1 - \lambda_2}^{J_0^*}(\phi, \theta, 0) \quad (\text{A.2})$$

and the energy depended part H_{λ_1, λ_2} . The rotation operator gives a clear definition of λ_1 and λ_2 that the z -axis is the direction of \vec{p}_1 in the rest frame of p_0 , which can be denoted as Euler rotation $R(\phi, \theta, 0)$. In sequence decay, all rotation from initial state to the final states should be considered.

In our $\Lambda_c^+ \rightarrow \Lambda\pi^+\pi^0, \Lambda \rightarrow p\pi^-$ process, there are three decay chains, which have been shown in figure 4. Following the rotation sequence, we can get the expressions below.

- For the decay chain $\Lambda_c^+ \rightarrow \Lambda\rho(770)^+$, the rotation is expressed as:

$$R_\rho = R(\phi_p^{\Lambda_1}, \theta_{\Lambda_1}, 0)B_z(p_{\Lambda_c^+}^{\Lambda_1})R_x(\pi)R(\phi_{\Lambda_c^+}^1, \theta_{\Lambda_c^+}^1, 0), \quad (\text{A.3})$$

where the Euler rotation $R(\phi, \theta, 0)$ can be expanded as $R_y(\theta)R_z(\phi)$, B_z denotes boost operation and $R_x(\pi)$ part means rotation from $\rho(770)^+$ direction to the Λ direction, where the rotation $R_x(\pi)$ will satisfy the relation $R_x(\pi)R(\phi, \theta, 0) = R(\phi - \pi, \pi - \theta, 0)$.

- For $\Lambda_c^+ \rightarrow \Sigma^{*+}\pi^0$, it is expressed as:

$$R_{\Sigma^{*+}} = R(\phi_p^{\Lambda_2}, \theta_{\Lambda_2}, 0)B_z(p_{\Lambda_c^+}^{\Sigma^{*+}})R(\phi_{\Lambda_c^+}^{\Sigma^{*+}}, \theta_{\Sigma^{*+}}, 0)B_z(p_{\Sigma^{*+}})R(\phi_{\Lambda_c^+}^2, \theta_{\Lambda_c^+}^2, 0). \quad (\text{A.4})$$

- For $\Lambda_c^+ \rightarrow \Sigma^{*0}\pi^+$, it is expressed as:

$$R_{\Sigma^{*0}} = R(\phi_p^{\Lambda_3}, \theta_{\Lambda_3}, 0)B_z(p_{\Lambda_c^+}^{\Sigma^{*0}})R(\phi_{\Lambda_c^+}^{\Sigma^{*0}}, \theta_{\Sigma^{*0}}, 0)B_z(p_{\Sigma^{*0}})R(\phi_{\Lambda_c^+}^3, \theta_{\Lambda_c^+}^3, 0). \quad (\text{A.5})$$

When we take the decay chain $\Lambda_c^+ \rightarrow \Lambda\rho(770)^+$ as a reference chain, the rotation of alignment is defined as:

$$R_{\Sigma^{*+}}^{\text{align}} = R_\rho R_{\Sigma^{*+}}^{-1}, \quad R_{\Sigma^{*0}}^{\text{align}} = R_\rho R_{\Sigma^{*0}}^{-1}. \quad (\text{A.6})$$

Using the 2-dimensional representation of SU(2) group, the rotation and boost operations can be expressed with:

$$R_z(\phi) = \begin{pmatrix} e^{-i\frac{\phi}{2}} & 0 \\ 0 & e^{i\frac{\phi}{2}} \end{pmatrix}, \quad R_y(\theta) = \begin{pmatrix} \cos\frac{\theta}{2} & -\sin\frac{\theta}{2} \\ \sin\frac{\theta}{2} & \cos\frac{\theta}{2} \end{pmatrix}, \quad B_z(\omega) = \begin{pmatrix} e^{-\omega/2} & 0 \\ 0 & e^{\omega/2} \end{pmatrix}, \quad (\text{A.7})$$

where $\omega = \text{arccosh}\left(\frac{1}{\sqrt{1-(\frac{p}{E})^2}}\right)$, we can convert R_i^{align} into several rotations with Euler angles which are the expected alignment angles and can be solved with the equations:

$$R_{\Sigma^{*+}}^{\text{align}} = B_z(\omega)R_z(\gamma_p)R_y(\beta_p)R_z(\alpha_p), \quad R_{\Sigma^{*0}}^{\text{align}} = B_z(\omega')R_z(\gamma'_p)R_y(\beta'_p)R_z(\alpha'_p). \quad (\text{A.8})$$

Acknowledgments

The BESIII collaboration thanks the staff of BEPCII and the IHEP computing center for their strong support. This work is supported in part by National Key R&D Program of China under Contracts Nos. 2020YFA0406400, 2020YFA0406300; National Natural Science Foundation of China (NSFC) under Contracts Nos. 11635010, 11735014, 11835012, 11935015, 11935016, 11935018, 11961141012, 12022510, 12025502, 12035009, 12035013, 12192260, 12192261, 12192262, 12192263, 12192264, 12192265, 12221005; the Chinese Academy of Sciences (CAS) Large-Scale Scientific Facility Program; Joint Large-Scale Scientific Facility Funds of the NSFC and CAS under Contract No. U1832207; the CAS Center for Excellence in Particle Physics (CCEPP); 100 Talents Program of CAS; Fundamental Research Funds for the Central Universities, Lanzhou University, University of Chinese Academy of Sciences; The Institute of Nuclear and Particle Physics (INPAC) and Shanghai Key Laboratory for Particle Physics and Cosmology; ERC under Contract No. 758462; European Union's Horizon 2020 research and innovation programme under Marie Skłodowska-Curie grant agreement under Contract No. 894790; German Research Foundation DFG under Contracts Nos. 443159800, Collaborative Research Center CRC 1044, GRK 2149; Istituto Nazionale di Fisica Nucleare, Italy; Ministry of Development of Turkey under Contract No. DPT2006K-120470; National Science and Technology fund; National Science Research and Innovation Fund (NSRF) via the Program Management Unit for Human Resources & Institutional Development, Research and Innovation under Contract No. B16F640076; STFC (United Kingdom); Suranaree University of Technology (SUT), Thailand Science Research and Innovation (TSRI), and National Science Research and Innovation Fund (NSRF) under Contract No. 160355; The Royal Society, U.K. under Contracts Nos. DH140054, DH160214; The Swedish Research Council; U.S. Department of Energy under Contract No. DE-FG02-05ER41374.

Open Access. This article is distributed under the terms of the Creative Commons Attribution License ([CC-BY 4.0](https://creativecommons.org/licenses/by/4.0/)), which permits any use, distribution and reproduction in any medium, provided the original author(s) and source are credited. SCOAP³ supports the goals of the International Year of Basic Sciences for Sustainable Development.

References

- [1] G.S. Abrams et al., *Observation of charmed baryon production in e^+e^- Annihilation*, *Phys. Rev. Lett.* **44** (1980) 10 [[INSPIRE](#)].
- [2] BESIII collaboration, *Determination of the Λ_c^+ spin via the reaction $e^+e^- \rightarrow \Lambda_c^+ \bar{\Lambda}_c^-$* , *Phys. Rev. D* **103** (2021) L091101 [[arXiv:2011.00396](#)] [[INSPIRE](#)].
- [3] H.-Y. Cheng, *Charmed baryons circa 2015*, *Front. Phys. (Beijing)* **10** (2015) 101406 [[INSPIRE](#)].
- [4] H.Y. Cheng, *Charmed baryon physics circa 2021*, *Chin. J. Phys.* **78** (2022) 324.
- [5] H.B. Li and X.R. Lyu, *Study of the standard model with weak decays of charmed hadrons at BESIII*, *Natl. Sci. Rev.* **8** (2021) nwab181.
- [6] LHCb collaboration, *Measurement of the Ω_c^0 baryon lifetime*, *Phys. Rev. Lett.* **121** (2018) 092003 [[arXiv:1807.02024](#)] [[INSPIRE](#)].

- [7] LHCb collaboration, *Precision measurement of the Λ_c^+ , Ξ_c^+ and Ξ_c^0 baryon lifetimes*, *Phys. Rev. D* **100** (2019) 032001 [[arXiv:1906.08350](#)] [[INSPIRE](#)].
- [8] LHCb collaboration, *Measurement of the lifetimes of promptly produced Ω_c^0 and Ξ_c^0 baryons*, *Sci. Bull.* **67** (2022) 479.
- [9] H.Y. Cheng, *The strangest lifetime: a bizarre story of $\tau(\Omega_c^0)$* , *Sci. Bull.* **67** (2022) 445.
- [10] BESIII collaboration, *Measurements of absolute hadronic branching fractions of Λ_c^+ baryon*, *Phys. Rev. Lett.* **116** (2016) 052001 [[arXiv:1511.08380](#)] [[INSPIRE](#)].
- [11] PARTICLE DATA GROUP collaboration, *Review of Particle Physics*, *PTEP* **2020** (2020) 083C01 [[INSPIRE](#)].
- [12] CLEO collaboration, *Observation of Λ_c^+ decays to $\Lambda\pi^+\pi^0$, $\Sigma^0\pi^+$, $\Sigma^0\pi^+\pi^0$, and $\Sigma^0\pi^-\pi^+\pi^+$* , *Phys. Lett. B* **325** (1994) 257 [[INSPIRE](#)].
- [13] C.Q. Geng, C.-W. Liu and T.-H. Tsai, *Charmed Baryon Weak Decays with Vector Mesons*, *Phys. Rev. D* **101** (2020) 053002 [[arXiv:2001.05079](#)] [[INSPIRE](#)].
- [14] H.-Y. Cheng and B. Tseng, *Nonleptonic weak decays of charmed baryons*, *Phys. Rev. D* **46** (1992) 1042 [*Erratum ibid.* **55** (1997) 1697] [[INSPIRE](#)].
- [15] H.Y. Cheng and B. Tseng, *Erratum: Nonleptonic weak decays of charmed baryons*, *Phys. Rev. D* **55** (1997) 1697.
- [16] Y.K. Hsiao, Q. Yi, S.-T. Cai and H.J. Zhao, *Two-body charmed baryon decays involving decuplet baryon in the quark-diagram scheme*, *Eur. Phys. J. C* **80** (2020) 1067 [[arXiv:2006.15291](#)] [[INSPIRE](#)].
- [17] C.-Q. Geng, C.-W. Liu, T.-H. Tsai and Y. Yu, *Charmed baryon weak decays with decuplet baryon and SU(3) flavor symmetry*, *Phys. Rev. D* **99** (2019) 114022 [[arXiv:1904.11271](#)] [[INSPIRE](#)].
- [18] K. Miura and T. Minamikawa, *Nonleptonic Hyperon Decay in the Quark Model*, *Prog. Theor. Phys.* **38** (1967) 954 [[INSPIRE](#)].
- [19] J.G. Korner, *Octet behaviour of single-particle matrix elements $\langle B'|Hw|B\rangle$ and $\langle M'|Hw|M\rangle$ using a weak current current quark Hamiltonian*, *Nucl. Phys. B* **25** (1971) 282 [[INSPIRE](#)].
- [20] J.G. Korner, *Spin, helicity and flavor patterns in exclusive decays of bottom mesons into baryon-antibaryon pairs*, *Z. Phys. C* **43** (1989) 165 [[INSPIRE](#)].
- [21] J.C. Pati and C.H. Woo, *$\Delta I = \frac{1}{2}$ rule with fermion quarks*, *Phys. Rev. D* **3** (1971) 2920 [[INSPIRE](#)].
- [22] BESIII collaboration, *Precision measurement of the integrated luminosity of the data taken by BESIII at center of mass energies between 3.810 GeV and 4.600 GeV*, *Chin. Phys. C* **39** (2015) 093001 [[arXiv:1503.03408](#)] [[INSPIRE](#)].
- [23] BESIII collaboration, *Luminosities and energies of e^+e^- collision data taken between $\sqrt{s} = 4.612$ GeV and 4.946 GeV at BESIII*, *Chin. Phys. C* **46** (2022) 113003 [[arXiv:2205.04809](#)] [[INSPIRE](#)].
- [24] BESIII collaboration, *Design and Construction of the BESIII Detector*, *Nucl. Instrum. Meth. A* **614** (2010) 345 [[arXiv:0911.4960](#)] [[INSPIRE](#)].
- [25] C.H. Yu et al., *BEPCII Performance and Beam Dynamics Studies on Luminosity*, in *Proc. of International Particle Accelerator Conference (IPAC'16)*, Busan, Korea, May 8–13, 2016, no. 7 in International Particle Accelerator Conference, Geneva, Switzerland, pp. 1014–1018, JACoW, June, 2016 [[doi:10.18429/JACoW-IPAC2016-TUYA01](#)].

- [26] D. Wang, R.-G. Ping, L. Li, X.-R. Lyu and Y.-H. Zheng, *Charmed baryon decay asymmetry in e^+e^- annihilation*, *Chin. Phys. C* **41** (2017) 023106 [[arXiv:1612.05918](#)] [[INSPIRE](#)].
- [27] BESIII collaboration, *Measurements of Weak Decay Asymmetries of $\Lambda_c^+ \rightarrow pK_S^0$, $\Lambda\pi^+$, $\Sigma^+\pi^0$, and $\Sigma^0\pi^+$* , *Phys. Rev. D* **100** (2019) 072004 [[arXiv:1905.04707](#)] [[INSPIRE](#)].
- [28] BESIII collaboration, *Future Physics Programme of BESIII*, *Chin. Phys. C* **44** (2020) 040001 [[arXiv:1912.05983](#)] [[INSPIRE](#)].
- [29] X. Li et al., *Study of MRPC technology for BESIII endcap-TOF upgrade*, *Radiat. Detect. Technol. Meth.* **1** (2017) 13.
- [30] Y.X. Guo et al., *The study of time calibration for upgraded end cap TOF of BESIII*, *Radiat. Detect. Technol. Meth.* **1** (2017) 15.
- [31] P. Cao et al., *Design and construction of the new BESIII endcap Time-of-Flight system with MRPC technology*, *Nucl. Instrum. Meth. A* **953** (2020) 163053.
- [32] GEANT4 collaboration, *Geant4 — a simulation toolkit*, *Nucl. Instrum. Meth. A* **506** (2003) 250 [[INSPIRE](#)].
- [33] Z.Y. You, Y.T. Liang and Y.J. Mao, *A method for detector description exchange among ROOT GEANT4 and GEANT3*, *Chin. Phys. C* **32** (2008) 572.
- [34] Y.-T. Liang et al., *A uniform geometry description for simulation, reconstruction and visualization in the BESIII experiment*, *Nucl. Instrum. Meth. A* **603** (2009) 325 [[INSPIRE](#)].
- [35] K.-X. Huang et al., *Method for detector description transformation to Unity and application in BESIII*, *Nucl. Sci. Tech.* **33** (2022) 142 [[arXiv:2206.10117](#)] [[INSPIRE](#)].
- [36] S. Jadach, B.F.L. Ward and Z. Was, *Coherent exclusive exponentiation for precision Monte Carlo calculations*, *Phys. Rev. D* **63** (2001) 113009 [[hep-ph/0006359](#)] [[INSPIRE](#)].
- [37] S. Jadach, B.F.L. Ward and Z. Was, *The Precision Monte Carlo event generator KK for two fermion final states in e^+e^- collisions*, *Comput. Phys. Commun.* **130** (2000) 260 [[hep-ph/9912214](#)] [[INSPIRE](#)].
- [38] D.J. Lange, *The EvtGen particle decay simulation package*, *Nucl. Instrum. Meth. A* **462** (2001) 152 [[INSPIRE](#)].
- [39] R.-G. Ping, *Event generators at BESIII*, *Chin. Phys. C* **32** (2008) 599 [[INSPIRE](#)].
- [40] J.C. Chen, G.S. Huang, X.R. Qi, D.H. Zhang and Y.S. Zhu, *Event generator for J/ψ and $\psi(2S)$ decay*, *Phys. Rev. D* **62** (2000) 034003 [[INSPIRE](#)].
- [41] R.-L. Yang, R.-G. Ping and H. Chen, *Tuning and Validation of the Lundcharm Model with J/ψ Decays*, *Chin. Phys. Lett.* **31** (2014) 061301 [[INSPIRE](#)].
- [42] E. Richter-Was, *QED bremsstrahlung in semileptonic B and leptonic tau decays*, *Phys. Lett. B* **303** (1993) 163 [[INSPIRE](#)].
- [43] Y. Guan, X.-R. Lü, Y. Zheng and Y.-F. Wang, *Study of the efficiency of event start time determination at BESIII*, *Chin. Phys. C* **38** (2014) 016201 [[arXiv:1304.6177](#)] [[INSPIRE](#)].
- [44] K.S. Cranmer, *Kernel estimation in high-energy physics*, *Comput. Phys. Commun.* **136** (2001) 198 [[hep-ex/0011057](#)] [[INSPIRE](#)].
- [45] ARGUS collaboration, *A partial wave analysis of the decay $D^0 \rightarrow K_S^0\pi^+\pi^-$* , *Phys. Lett. B* **308** (1993) 435 [[INSPIRE](#)].
- [46] Y. Jiang et al., *Open-source framework TF-PWA package*, GitHub link: <https://github.com/jiangyi15/tf-pwa> (2020).

- [47] M. Wang, Y. Jiang, Y. Liu, W. Qian, X. Lyu and L. Zhang, *A novel method to test particle ordering and final state alignment in helicity formalism*, *Chin. Phys. C* **45** (2021) 063103 [[arXiv:2012.03699](#)] [[INSPIRE](#)].
- [48] S.U. Chung, *A General formulation of covariant helicity coupling amplitudes*, *Phys. Rev. D* **57** (1998) 431 [[INSPIRE](#)].
- [49] F. Von Hippel and C. Quigg, *Centrifugal-barrier effects in resonance partial decay widths, shapes, and production amplitudes*, *Phys. Rev. D* **5** (1972) 624 [[INSPIRE](#)].
- [50] BESIII collaboration, *Partial wave analysis of $\psi(3686) \rightarrow K^+ K^- \eta$* , *Phys. Rev. D* **101** (2020) 032008 [[arXiv:1912.08566](#)] [[INSPIRE](#)].
- [51] G.J. Gounaris and J.J. Sakurai, *Finite width corrections to the vector meson dominance prediction for $\rho \rightarrow e^+ e^-$* , *Phys. Rev. Lett.* **21** (1968) 244 [[INSPIRE](#)].
- [52] C. Langenbruch, *Parameter uncertainties in weighted unbinned maximum likelihood fits*, *Eur. Phys. J. C* **82** (2022) 393 [[arXiv:1911.01303](#)] [[INSPIRE](#)].
- [53] A.V. Sarantsev, M. Matveev, V.A. Nikonov, A.V. Anisovich, U. Thoma and E. Klempt, *Hyperon II: Properties of excited hyperons*, *Eur. Phys. J. A* **55** (2019) 180 [[arXiv:1907.13387](#)] [[INSPIRE](#)].
- [54] M. Ablikim et al., *Polarization and entanglement in baryon-antibaryon pair production in electron-positron annihilation*, *Nature Phys.* **15** (2019) 631.
- [55] D.G. Ireland et al., *Kaon Photoproduction and the Λ Decay Parameter α_-* , *Phys. Rev. Lett.* **123** (2019) 182301 [[arXiv:1904.07616](#)] [[INSPIRE](#)].
- [56] BESIII collaboration, *Precise Measurements of Decay Parameters and CP Asymmetry with Entangled $\Lambda - \bar{\Lambda}$ Pairs*, *Phys. Rev. Lett.* **129** (2022) 131801 [[arXiv:2204.11058](#)] [[INSPIRE](#)].
- [57] J.G. Körner and M. Krämer, *Polarization effects in exclusive semi-leptonic Λ_c^+ and Λ_b^+ charm and bottom baryon decays*, *Phys. Lett. B* **275** (1992) 495 [[INSPIRE](#)].
- [58] M. Matveev, A.V. Sarantsev, V.A. Nikonov, A.V. Anisovich, U. Thoma and E. Klempt, *Hyperon I: Partial-wave amplitudes for $K^- p$ scattering*, *Eur. Phys. J. A* **55** (2019) 179 [[arXiv:1907.03645](#)] [[INSPIRE](#)].
- [59] BESIII collaboration, *Measurement of absolute branching fraction of the inclusive decay $\Lambda_c^+ \rightarrow \Lambda + X$* , *Phys. Rev. Lett.* **121** (2018) 062003 [[arXiv:1803.05706](#)] [[INSPIRE](#)].
- [60] BESIII collaboration, *Analysis of $D^+ \rightarrow \bar{K}^0 e^+ \nu_e$ and $D^+ \rightarrow \pi^0 e^+ \nu_e$ semileptonic decays*, *Phys. Rev. D* **96** (2017) 012002 [[arXiv:1703.09084](#)] [[INSPIRE](#)].
- [61] BESIII collaboration, *Model-Independent Determination of the Spin of the Ω^- and Its Polarization Alignment in $\psi(3686) \rightarrow \Omega^- \bar{\Omega}^+$* , *Phys. Rev. Lett.* **126** (2021) 092002 [[arXiv:2007.03679](#)] [[INSPIRE](#)].
- [62] M.R. Chernick, *Bootstrap methods: A guide for practitioners and researchers*, John Wiley & Sons, 2 edition (2007).

The BESIII collaboration

M. Ablikim¹, M.N. Achasov^{11,b}, P. Adlarson⁷⁰, M. Albrecht⁴, R. Aliberti³¹, A. Amoroso^{69A,69C}, M.R. An³⁵, Q. An^{66,53}, X.H. Bai⁶¹, Y. Bai⁵², O. Bakina³², R. Baldini Ferroli^{26A}, I. Balossino^{27A}, Y. Ban^{42,g}, V. Batozskaya^{1,40}, D. Becker³¹, K. Begzsuren²⁹, N. Berger³¹, M. Bertani^{26A}, D. Bettoni^{27A}, F. Bianchi^{69A,69C}, J. Bloms⁶³, A. Bortone^{69A,69C}, I. Boyko³², R.A. Briere⁵, A. Brueggemann⁶³, H. Cai⁷¹, X. Cai^{1,53}, A. Calcaterra^{26A}, G.F. Cao^{1,58}, N. Cao^{1,58}, S.A. Cetin^{57A}, J.F. Chang^{1,53}, W.L. Chang^{1,58}, G. Chelkov^{32,a}, C. Chen³⁹, Chao Chen⁵⁰, G. Chen¹, H.S. Chen^{1,58}, M.L. Chen^{1,53}, S.J. Chen³⁸, S.M. Chen⁵⁶, T. Chen¹, X.R. Chen^{28,58}, X.T. Chen¹, Y.B. Chen^{1,53}, Z.J. Chen^{23,h}, W.S. Cheng^{69C}, S.K. Choi⁵⁰, X. Chu³⁹, G. Cibinetto^{27A}, F. Cossio^{69C}, J.J. Cui⁴⁵, H.L. Dai^{1,53}, J.P. Dai⁷³, A. Dbeyssi¹⁷, R.E. de Boer⁴, D. Dedovich³², Z.Y. Deng¹, A. Denig³¹, I. Denysenko³², M. Destefanis^{69A,69C}, F. De Mori^{69A,69C}, Y. Ding³⁶, J. Dong^{1,53}, L.Y. Dong^{1,58}, M.Y. Dong^{1,53,58}, X. Dong⁷¹, S.X. Du⁷⁵, P. Egorov^{32,a}, Y.L. Fan⁷¹, J. Fang^{1,53}, S.S. Fang^{1,58}, W.X. Fang¹, Y. Fang¹, R. Farinelli^{27A}, L. Fava^{69B,69C}, F. Feldbauer⁴, G. Felici^{26A}, C.Q. Feng^{66,53}, J.H. Feng⁵⁴, K. Fischer⁶⁴, M. Fritsch⁴, C. Fritzschn⁶³, C.D. Fu¹, H. Gao⁵⁸, Y.N. Gao^{42,g}, Yang Gao^{66,53}, S. Garbolino^{69C}, I. Garzia^{27A,27B}, P.T. Ge⁷¹, Z.W. Ge³⁸, C. Geng⁵⁴, E.M. Gersabeck⁶², A. Gilman⁶⁴, K. Goetzen¹², L. Gong³⁶, W.X. Gong^{1,53}, W. Gradl³¹, M. Greco^{69A,69C}, L.M. Gu³⁸, M.H. Gu^{1,53}, Y.T. Gu¹⁴, C. Y Guan^{1,58}, A.Q. Guo^{28,58}, L.B. Guo³⁷, R.P. Guo⁴⁴, Y.P. Guo^{10,f}, A. Guskov^{32,a}, T.T. Han⁴⁵, W.Y. Han³⁵, X.Q. Hao¹⁸, F.A. Harris⁶⁰, K.K. He⁵⁰, K.L. He^{1,58}, F.H. Heinsius⁴, C.H. Heinz³¹, Y.K. Heng^{1,53,58}, C. Herold⁵⁵, G.Y. Hou^{1,58}, Y.R. Hou⁵⁸, Z.L. Hou¹, H.M. Hu^{1,58}, J.F. Hu^{51,i}, T. Hu^{1,53,58}, Y. Hu¹, G.S. Huang^{66,53}, K.X. Huang⁵⁴, L.Q. Huang^{28,58}, X.T. Huang⁴⁵, Y.P. Huang¹, Z. Huang^{42,g}, T. Hussain⁶⁸, N. Hüsken^{25,31}, W. Imoehl²⁵, M. Irshad^{66,53}, J. Jackson²⁵, S. Jaeger⁴, S. Janchiv²⁹, E. Jang⁵⁰, J.H. Jeong⁵⁰, Q. Ji¹, Q.P. Ji¹⁸, X.B. Ji^{1,58}, X.L. Ji^{1,53}, Y.Y. Ji⁴⁵, Z.K. Jia^{66,53}, H.B. Jiang⁴⁵, S.S. Jiang³⁵, X.S. Jiang^{1,53,58}, Y. Jiang⁵⁸, J.B. Jiao⁴⁵, Z. Jiao²¹, S. Jin³⁸, Y. Jin⁶¹, M.Q. Jing^{1,58}, T. Johansson⁷⁰, N. Kalantar-Nayestanaki⁵⁹, X.S. Kang³⁶, R. Kappert⁵⁹, M. Kavatsyuk⁵⁹, B.C. Ke⁷⁵, I.K. Keshk⁴, A. Khoukaz⁶³, R. Kiuchi¹, R. Kliemt¹², L. Koch³³, O.B. Kolcu^{57A}, B. Kopf⁴, M. Kuemmel⁴, M. Kuessner⁴, A. Kupsc^{40,70}, W. Kühn³³, J.J. Lane⁶², J.S. Lange³³, P. Larin¹⁷, A. Lavania²⁴, L. Lavezzi^{69A,69C}, Z.H. Lei^{66,53}, H. Leithoff³¹, M. Lellmann³¹, T. Lenz³¹, C. Li³⁹, C. Li⁴³, C.H. Li³⁵, Cheng Li^{66,53}, D.M. Li⁷⁵, F. Li^{1,53}, G. Li¹, H. Li⁴⁷, H. Li^{66,53}, H.B. Li^{1,58}, H.J. Li¹⁸, H.N. Li^{51,i}, J.Q. Li⁴, J.S. Li⁵⁴, J.W. Li⁴⁵, Ke Li¹, L. J Li¹, L.K. Li¹, Lei Li³, M.H. Li³⁹, P.R. Li^{34,j,k}, S.X. Li¹⁰, S.Y. Li⁵⁶, T. Li⁴⁵, W.D. Li^{1,58}, W.G. Li¹, X.H. Li^{66,53}, X.L. Li⁴⁵, Xiaoyu Li^{1,58}, Y.G. Li^{42,g}, Z.X. Li¹⁴, H. Liang^{66,53}, H. Liang³⁰, H. Liang^{1,58}, Y.F. Liang⁴⁹, Y.T. Liang^{28,58}, G.R. Liao¹³, L.Z. Liao⁴⁵, J. Libby²⁴, A. Limphirat⁵⁵, C.X. Lin⁵⁴, D.X. Lin^{28,58}, T. Lin¹, B.J. Liu¹, C.X. Liu¹, D. Liu^{17,66}, F.H. Liu⁴⁸, Fang Liu¹, Feng Liu⁶, G.M. Liu^{51,i}, H. Liu^{34,j,k}, H.B. Liu¹⁴, H.M. Liu^{1,58}, Huanhuan Liu¹, Huihui Liu¹⁹, J.B. Liu^{66,53}, J.L. Liu⁶⁷, J.Y. Liu^{1,58}, K. Liu¹, K.Y. Liu³⁶, Ke Liu²⁰, L. Liu^{66,53}, Lu Liu³⁹, M.H. Liu^{10,f}, P.L. Liu¹, Q. Liu⁵⁸, S.B. Liu^{66,53}, T. Liu^{10,f}, W.K. Liu³⁹, W.M. Liu^{66,53}, X. Liu^{34,j,k}, Y. Liu^{34,j,k}, Y.B. Liu³⁹, Z.A. Liu^{1,53,58}, Z.Q. Liu⁴⁵, X.C. Lou^{1,53,58}, F.X. Lu⁵⁴, H.J. Lu²¹, J.G. Lu^{1,53}, X.L. Lu¹, Y. Lu⁷, Y.P. Lu^{1,53}, Z.H. Lu¹, C.L. Luo³⁷, M.X. Luo⁷⁴, T. Luo^{10,f}, X.L. Luo^{1,53}, X.R. Lyu⁵⁸, Y.F. Lyu³⁹, F.C. Ma³⁶, H.L. Ma¹, L.L. Ma⁴⁵, M.M. Ma^{1,58}, Q.M. Ma¹, R.Q. Ma^{1,58}, R.T. Ma⁵⁸, X.Y. Ma^{1,53}, Y. Ma^{42,g}, F.E. Maas¹⁷, M. Maggiora^{69A,69C}, S. Maldaner⁴, S. Malde⁶⁴, Q.A. Malik⁶⁸, A. Mangoni^{26B}, Y.J. Mao^{42,g}, Z.P. Mao¹, S. Marcello^{69A,69C}, Z.X. Meng⁶¹, J. Messchendorp^{12,59}, G. Mezzadri^{27A}, H. Miao¹, T.J. Min³⁸, R.E. Mitchell²⁵, X.H. Mo^{1,53,58}, N. Yu. Muchnoi^{11,b}, Y. Nefedov³², F. Nerling^{17,d}, I.B. Nikolaev^{11,b}, Z. Ning^{1,53}, S. Nisar^{9,l}, Y. Niu⁴⁵, S.L. Olsen⁵⁸, Q. Ouyang^{1,53,58}, S. Pacetti^{26B,26C}, X. Pan^{10,f}, Y. Pan⁵², A. Pathak³⁰, M. Pelizaeus⁴, H.P. Peng^{66,53}, K. Peters^{12,d}, J.L. Ping³⁷, R.G. Ping^{1,58}, S. Plura³¹, S. Pogodin³², V. Prasad^{66,53}, F.Z. Qi¹, H. Qi^{66,53}, H.R. Qi⁵⁶, M. Qi³⁸, T.Y. Qi^{10,f}, S. Qian^{1,53}, W.B. Qian⁵⁸, Z. Qian⁵⁴,

C.F. Qiao⁵⁸, J.J. Qin⁶⁷, L.Q. Qin¹³, X.P. Qin^{10,f}, X.S. Qin⁴⁵, Z.H. Qin^{1,53}, J.F. Qiu¹, S.Q. Qu⁵⁶, K.H. Rashid⁶⁸, C.F. Redmer³¹, K.J. Ren³⁵, A. Rivetti^{69C}, V. Rodin⁵⁹, M. Rolo^{69C}, G. Rong^{1,58}, Ch. Rosner¹⁷, S.N. Ruan³⁹, H.S. Sang⁶⁶, A. Sarantsev^{32,c}, Y. Schelhaas³¹, C. Schmier⁴, K. Schoenning⁷⁰, M. Scodeggio^{27A,27B}, K.Y. Shan^{10,f}, W. Shan²², X.Y. Shan^{66,53}, J.F. Shangguan⁵⁰, L.G. Shao^{1,58}, M. Shao^{66,53}, C.P. Shen^{10,f}, H.F. Shen^{1,58}, X.Y. Shen^{1,58}, B.A. Shi⁵⁸, H.C. Shi^{66,53}, J.Y. Shi¹, Q.Q. Shi⁵⁰, R.S. Shi^{1,58}, X. Shi^{1,53}, X. D Shi^{66,53}, J.J. Song¹⁸, W.M. Song^{30,1}, Y.X. Song^{42,g}, S. Sosio^{69A,69C}, S. Spataro^{69A,69C}, F. Stieler³¹, K.X. Su⁷¹, P.P. Su⁵⁰, Y.J. Su⁵⁸, G.X. Sun¹, H. Sun⁵⁸, H.K. Sun¹, J.F. Sun¹⁸, L. Sun⁷¹, S.S. Sun^{1,58}, T. Sun^{1,58}, W.Y. Sun³⁰, X. Sun^{23,h}, Y.J. Sun^{66,53}, Y.Z. Sun¹, Z.T. Sun⁴⁵, Y.H. Tan⁷¹, Y.X. Tan^{66,53}, C.J. Tang⁴⁹, G.Y. Tang¹, J. Tang⁵⁴, L. Y. Tao⁶⁷, Q.T. Tao^{23,h}, M. Tat⁶⁴, J.X. Teng^{66,53}, V. Thoren⁷⁰, W.H. Tian⁴⁷, Y. Tian^{28,58}, I. Uman^{57B}, B. Wang¹, B.L. Wang⁵⁸, C.W. Wang³⁸, D.Y. Wang^{42,g}, F. Wang⁶⁷, H.J. Wang^{34,j,k}, H.P. Wang^{1,58}, K. Wang^{1,53}, L.L. Wang¹, M. Wang⁴⁵, M.Z. Wang^{42,g}, Meng Wang^{1,58}, S. Wang¹³, S. Wang^{10,f}, T. Wang^{10,f}, T.J. Wang³⁹, W. Wang⁵⁴, W.H. Wang⁷¹, W.P. Wang^{66,53}, X. Wang^{42,g}, X.F. Wang^{34,j,k}, X.L. Wang^{10,f}, Y. Wang⁵⁶, Y.D. Wang⁴¹, Y.F. Wang^{1,53,58}, Y.H. Wang⁴³, Y.Q. Wang¹, Yaqian Wang^{16,1}, Z. Wang^{1,53}, Z.Y. Wang^{1,58}, Ziyi Wang⁵⁸, D.H. Wei¹³, F. Weidner⁶³, S.P. Wen¹, D.J. White⁶², U. Wiedner⁴, G. Wilkinson⁶⁴, M. Wolke⁷⁰, L. Wollenberg⁴, J.F. Wu^{1,58}, L.H. Wu¹, L.J. Wu^{1,58}, X. Wu^{10,f}, X.H. Wu³⁰, Y. Wu⁶⁶, Y. J. Wu²⁸, Z. Wu^{1,53}, L. Xia^{66,53}, T. Xiang^{42,g}, D. Xiao^{34,j,k}, G.Y. Xiao³⁸, H. Xiao^{10,f}, S.Y. Xiao¹, Y.L. Xiao^{10,f}, Z.J. Xiao³⁷, C. Xie³⁸, X.H. Xie^{42,g}, Y. Xie⁴⁵, Y.G. Xie^{1,53}, Y.H. Xie⁶, Z.P. Xie^{66,53}, T.Y. Xing^{1,58}, C.F. Xu¹, C.J. Xu⁵⁴, G.F. Xu¹, H.Y. Xu⁶¹, Q.J. Xu¹⁵, X.P. Xu⁵⁰, Y.C. Xu⁵⁸, Z.P. Xu³⁸, F. Yan^{10,f}, L. Yan^{10,f}, W.B. Yan^{66,53}, W.C. Yan⁷⁵, H.J. Yang^{46,e}, H.L. Yang³⁰, H.X. Yang¹, L. Yang⁴⁷, S.L. Yang⁵⁸, Tao Yang¹, Y.F. Yang³⁹, Y.X. Yang^{1,58}, Yifan Yang^{1,58}, M. Ye^{1,53}, M.H. Ye⁸, J.H. Yin¹, Z.Y. You⁵⁴, B.X. Yu^{1,53,58}, C.X. Yu³⁹, G. Yu^{1,58}, T. Yu⁶⁷, X.D. Yu^{42,g}, C.Z. Yuan^{1,58}, L. Yuan², S.C. Yuan¹, X.Q. Yuan¹, Y. Yuan^{1,58}, Z.Y. Yuan⁵⁴, C.X. Yue³⁵, A.A. Zafar⁶⁸, F.R. Zeng⁴⁵, X. Zeng Zeng⁶, Y. Zeng^{23,h}, Y.H. Zhan⁵⁴, A.Q. Zhang¹, B.L. Zhang¹, B.X. Zhang¹, D.H. Zhang³⁹, G.Y. Zhang¹⁸, H. Zhang⁶⁶, H.H. Zhang³⁰, H.H. Zhang⁵⁴, H.Y. Zhang^{1,53}, J.L. Zhang⁷², J.Q. Zhang³⁷, J.W. Zhang^{1,53,58}, J.X. Zhang^{34,j,k}, J.Y. Zhang¹, J.Z. Zhang^{1,58}, Jianyu Zhang^{1,58}, Jiawei Zhang^{1,58}, L.M. Zhang⁵⁶, L.Q. Zhang⁵⁴, Lei Zhang³⁸, P. Zhang¹, Q.Y. Zhang^{35,75}, Shuihan Zhang^{1,58}, Shulei Zhang^{23,h}, X.D. Zhang⁴¹, X.M. Zhang¹, X.Y. Zhang⁴⁵, X.Y. Zhang⁵⁰, Y. Zhang⁶⁴, Y.T. Zhang⁷⁵, Y.H. Zhang^{1,53}, Yan Zhang^{66,53}, Yao Zhang¹, Z.H. Zhang¹, Z.Y. Zhang³⁹, Z.Y. Zhang⁷¹, G. Zhao¹, J. Zhao³⁵, J.Y. Zhao^{1,58}, J.Z. Zhao^{1,53}, Lei Zhao^{66,53}, Ling Zhao¹, M.G. Zhao³⁹, S.J. Zhao⁷⁵, Y.B. Zhao^{1,53}, Y.X. Zhao^{28,58}, Z.G. Zhao^{66,53}, A. Zhemchugov^{32,a}, B. Zheng⁶⁷, J.P. Zheng^{1,53}, Y.H. Zheng⁵⁸, B. Zhong³⁷, C. Zhong⁶⁷, X. Zhong⁵⁴, H. Zhou⁴⁵, L.P. Zhou^{1,58}, X. Zhou⁷¹, X.K. Zhou⁵⁸, X.R. Zhou^{66,53}, X.Y. Zhou³⁵, Y.Z. Zhou^{10,f}, J. Zhu³⁹, K. Zhu¹, K.J. Zhu^{1,53,58}, L.X. Zhu⁵⁸, S.H. Zhu⁶⁵, S.Q. Zhu³⁸, T.J. Zhu⁷², W.J. Zhu^{10,f}, Y.C. Zhu^{66,53}, Z.A. Zhu^{1,58}, J.H. Zou¹

¹ Institute of High Energy Physics, Beijing 100049, People's Republic of China

² Beihang University, Beijing 100191, People's Republic of China

³ Beijing Institute of Petrochemical Technology, Beijing 102617, People's Republic of China

⁴ Bochum Ruhr-University, D-44780 Bochum, Germany

⁵ Carnegie Mellon University, Pittsburgh, Pennsylvania 15213, U.S.A.

⁶ Central China Normal University, Wuhan 430079, People's Republic of China

⁷ Central South University, Changsha 410083, People's Republic of China

⁸ China Center of Advanced Science and Technology, Beijing 100190, People's Republic of China

⁹ COMSATS University Islamabad, Lahore Campus, Defence Road, Off Raiwind Road, 54000 Lahore, Pakistan

¹⁰ Fudan University, Shanghai 200433, People's Republic of China

¹¹ G.I. Budker Institute of Nuclear Physics SB RAS (BINP), Novosibirsk 630090, Russia

- ¹² GSI Helmholtzcentre for Heavy Ion Research GmbH, D-64291 Darmstadt, Germany
- ¹³ Guangxi Normal University, Guilin 541004, People's Republic of China
- ¹⁴ Guangxi University, Nanning 530004, People's Republic of China
- ¹⁵ Hangzhou Normal University, Hangzhou 310036, People's Republic of China
- ¹⁶ Hebei University, Baoding 071002, People's Republic of China
- ¹⁷ Helmholtz Institute Mainz, Staudinger Weg 18, D-55099 Mainz, Germany
- ¹⁸ Henan Normal University, Xinxiang 453007, People's Republic of China
- ¹⁹ Henan University of Science and Technology, Luoyang 471003, People's Republic of China
- ²⁰ Henan University of Technology, Zhengzhou 450001, People's Republic of China
- ²¹ Huangshan College, Huangshan 245000, People's Republic of China
- ²² Hunan Normal University, Changsha 410081, People's Republic of China
- ²³ Hunan University, Changsha 410082, People's Republic of China
- ²⁴ Indian Institute of Technology Madras, Chennai 600036, India
- ²⁵ Indiana University, Bloomington, Indiana 47405, U.S.A.
- ²⁶ INFN Laboratori Nazionali di Frascati, (A)INFN Laboratori Nazionali di Frascati, I-00044, Frascati, Italy; (B)INFN Sezione di Perugia, I-06100, Perugia, Italy; (C)University of Perugia, I-06100, Perugia, Italy
- ²⁷ INFN Sezione di Ferrara, (A)INFN Sezione di Ferrara, I-44122, Ferrara, Italy; (B)University of Ferrara, I-44122, Ferrara, Italy
- ²⁸ Institute of Modern Physics, Lanzhou 730000, People's Republic of China
- ²⁹ Institute of Physics and Technology, Peace Avenue 54B, Ulaanbaatar 13330, Mongolia
- ³⁰ Jilin University, Changchun 130012, People's Republic of China
- ³¹ Johannes Gutenberg University of Mainz, Johann-Joachim-Becher-Weg 45, D-55099 Mainz, Germany
- ³² Joint Institute for Nuclear Research, 141980 Dubna, Moscow region, Russia
- ³³ Justus-Liebig-Universitaet Giessen, II. Physikalisches Institut, Heinrich-Buff-Ring 16, D-35392 Giessen, Germany
- ³⁴ Lanzhou University, Lanzhou 730000, People's Republic of China
- ³⁵ Liaoning Normal University, Dalian 116029, People's Republic of China
- ³⁶ Liaoning University, Shenyang 110036, People's Republic of China
- ³⁷ Nanjing Normal University, Nanjing 210023, People's Republic of China
- ³⁸ Nanjing University, Nanjing 210093, People's Republic of China
- ³⁹ Nankai University, Tianjin 300071, People's Republic of China
- ⁴⁰ National Centre for Nuclear Research, Warsaw 02-093, Poland
- ⁴¹ North China Electric Power University, Beijing 102206, People's Republic of China
- ⁴² Peking University, Beijing 100871, People's Republic of China
- ⁴³ Qufu Normal University, Qufu 273165, People's Republic of China
- ⁴⁴ Shandong Normal University, Jinan 250014, People's Republic of China
- ⁴⁵ Shandong University, Jinan 250100, People's Republic of China
- ⁴⁶ Shanghai Jiao Tong University, Shanghai 200240, People's Republic of China
- ⁴⁷ Shanxi Normal University, Linfen 041004, People's Republic of China
- ⁴⁸ Shanxi University, Taiyuan 030006, People's Republic of China
- ⁴⁹ Sichuan University, Chengdu 610064, People's Republic of China
- ⁵⁰ Soochow University, Suzhou 215006, People's Republic of China
- ⁵¹ South China Normal University, Guangzhou 510006, People's Republic of China
- ⁵² Southeast University, Nanjing 211100, People's Republic of China
- ⁵³ State Key Laboratory of Particle Detection and Electronics, Beijing 100049, Hefei 230026, People's Republic of China
- ⁵⁴ Sun Yat-Sen University, Guangzhou 510275, People's Republic of China
- ⁵⁵ Suranaree University of Technology, University Avenue 111, Nakhon Ratchasima 30000, Thailand
- ⁵⁶ Tsinghua University, Beijing 100084, People's Republic of China
- ⁵⁷ Turkish Accelerator Center Particle Factory Group, (A)Istinye University, 34010, Istanbul, Turkey; (B)Near East University, Nicosia, North Cyprus, Mersin 10, Turkey

- ⁵⁸ *University of Chinese Academy of Sciences, Beijing 100049, People’s Republic of China*
- ⁵⁹ *University of Groningen, NL-9747 AA Groningen, The Netherlands*
- ⁶⁰ *University of Hawaii, Honolulu, Hawaii 96822, U.S.A.*
- ⁶¹ *University of Jinan, Jinan 250022, People’s Republic of China*
- ⁶² *University of Manchester, Oxford Road, Manchester, M13 9PL, United Kingdom*
- ⁶³ *University of Muenster, Wilhelm-Klemm-Strasse 9, 48149 Muenster, Germany*
- ⁶⁴ *University of Oxford, Keble Road, Oxford OX13RH, United Kingdom*
- ⁶⁵ *University of Science and Technology Liaoning, Anshan 114051, People’s Republic of China*
- ⁶⁶ *University of Science and Technology of China, Hefei 230026, People’s Republic of China*
- ⁶⁷ *University of South China, Hengyang 421001, People’s Republic of China*
- ⁶⁸ *University of the Punjab, Lahore-54590, Pakistan*
- ⁶⁹ *University of Turin and INFN, (A)University of Turin, I-10125, Turin, Italy; (B)University of Eastern Piedmont, I-15121, Alessandria, Italy; (C)INFN, I-10125, Turin, Italy*
- ⁷⁰ *Uppsala University, Box 516, SE-75120 Uppsala, Sweden*
- ⁷¹ *Wuhan University, Wuhan 430072, People’s Republic of China*
- ⁷² *Xinyang Normal University, Xinyang 464000, People’s Republic of China*
- ⁷³ *Yunnan University, Kunming 650500, People’s Republic of China*
- ⁷⁴ *Zhejiang University, Hangzhou 310027, People’s Republic of China*
- ⁷⁵ *Zhengzhou University, Zhengzhou 450001, People’s Republic of China*
- ^a *Also at the Moscow Institute of Physics and Technology, Moscow 141700, Russia*
- ^b *Also at the Novosibirsk State University, Novosibirsk, 630090, Russia*
- ^c *Also at the NRC “Kurchatov Institute”, PNPI, 188300, Gatchina, Russia*
- ^d *Also at Goethe University Frankfurt, 60323 Frankfurt am Main, Germany*
- ^e *Also at Key Laboratory for Particle Physics, Astrophysics and Cosmology, Ministry of Education; Shanghai Key Laboratory for Particle Physics and Cosmology; Institute of Nuclear and Particle Physics, Shanghai 200240, People’s Republic of China*
- ^f *Also at Key Laboratory of Nuclear Physics and Ion-beam Application (MOE) and Institute of Modern Physics, Fudan University, Shanghai 200443, People’s Republic of China*
- ^g *Also at State Key Laboratory of Nuclear Physics and Technology, Peking University, Beijing 100871, People’s Republic of China*
- ^h *Also at School of Physics and Electronics, Hunan University, Changsha 410082, China*
- ⁱ *Also at Guangdong Provincial Key Laboratory of Nuclear Science, Institute of Quantum Matter, South China Normal University, Guangzhou 510006, China*
- ^j *Also at Frontiers Science Center for Rare Isotopes, Lanzhou University, Lanzhou 730000, People’s Republic of China*
- ^k *Also at Lanzhou Center for Theoretical Physics, Lanzhou University, Lanzhou 730000, People’s Republic of China*
- ^l *Also at the Department of Mathematical Sciences, IBA, Karachi, Pakistan*